

Chapter 4

Dynamical simulations of pump-probe ionization spectroscopy: Analysis and control

Sections 4.1 to 4.4 carefully analyze the dynamics in the lowest excited singlet states (b^1A' , c^1A' , a^1A'' , b^1A'') induced by a single laser pulse (= pump). Since only pump laser energies which are in the experimental range (3.1 - 3.6 eV) are considered, the energetically higher neutral states (>3.6 eV), which do not affect the pump-probe spectrum, are excluded in the theoretical computations of this chapter. Pump pulses within this scale only populate the two lowest excited states in each symmetry.

Attention is directed particularly to the influence of the nonadiabatic coupling. In section 4.1 it is shown, in both the adiabatic and the diabatic representation, how the coupling between the two lowest states of A'' symmetry, a^1A'' and b^1A'' , strongly influences the population dynamics, whereas the coupling between the b^1A' and the c^1A' states induces only marginal population transfer.

The calculation of the absorption spectrum (section 4.2) and the probability of fast (lifetime $\tau \approx$ pulse duration) dissociation (section 4.3) have been performed with the help of δ -pulses (equation (2.65)). Otherwise, \sin^2 -shaped pump and probe laser pulses are employed to photoexcite or ionize the molecule. The general form of these pulses is given by:

$$\epsilon_{x/y/z}(t) = \begin{cases} \epsilon_{x/y/z}^0 \cos(\omega t) \cdot \sin^2\left(\frac{\pi t}{t_{pulse}}\right) & : 0 < t < t_{pulse} \\ 0 & : \text{else} \end{cases}, \quad (4.1)$$

where t_{pulse} denotes the pulse duration, $\epsilon_{x/y/z}^0$ the amplitude and ω the frequency of the pulse which is linearly polarized in x-, y- or z-direction.

In the last part of this chapter (section 4.5), an *analysis* of the experimental pump-probe transient spectra and a *control* mechanism are proposed based on

time-dependent wave packets. In the pump-probe simulations, besides the five lowest neutral singlet states, a^1A' , b^1A' , c^1A' , a^1A'' and b^1A'' , the three lowest ionic doublet states, $(a^2A'')^+$, $(a^2A')^+$, $(b^2A')^+$, are included.

As pointed out in section 2.7, dynamical calculations including kinetic couplings call for the SOD scheme which usually demands a smaller time step than the split operator. In this case, a time step of 0.008 fs on a 1024 points grid was used. All propagations without kinetic coupling have been performed using the split operator technique in a grid of 1024 points with a time step 0.02 fs.

4.1 Influence of the diabatic b^1A' - c^1A' and a^1A'' - b^1A'' coupling on the dynamics

Neglecting nonadiabatic couplings, if the pump pulse prepares a state completely localized in the weakly bound c^1A' state or in the strongly bound b^1A'' state (see figure 4.1) no dissociation should occur and only a signal for the parent ion, $\text{CpMn}(\text{CO})_3^+$, should be observed after the probe pulse. Therefore, the question is whether the nonadiabatic coupling is strong enough to induce significant population transfer to the dissociative b^1A' or a^1A'' states, respectively. A second (= "probe") pulse could then prepare the daughter ion, $\text{CpMn}(\text{CO})_2^+$, provided the dissociating wavepackets on the b^1A' or the a^1A'' potential have enough kinetic energy (according to the Franck-Condon principle the momentum is conserved) to overcome the barrier in the ionic state.

For symmetry reasons the A' excited states are only populated by y- or z-linearly-polarized pump pulses whereas the A'' states can only be reached using x-linearly-polarized light. Consequently, two different pump-probe mechanisms can be predicted (see panels (a) and (b) in figure 4.1), that is, depending on the laser polarization, either the A' or the A'' states are populated by the pump pulse. No selection rules hold for the transition from the excited neutral to the ionic states. Hence, the ionic states are equally populated by x-, y- or z-polarized probe pulses. Both processes shown in figure 4.1 involve six (three neutral and three ionic) states and thus they are described by 6×6 -matrices in both the adiabatic and diabatic pic-

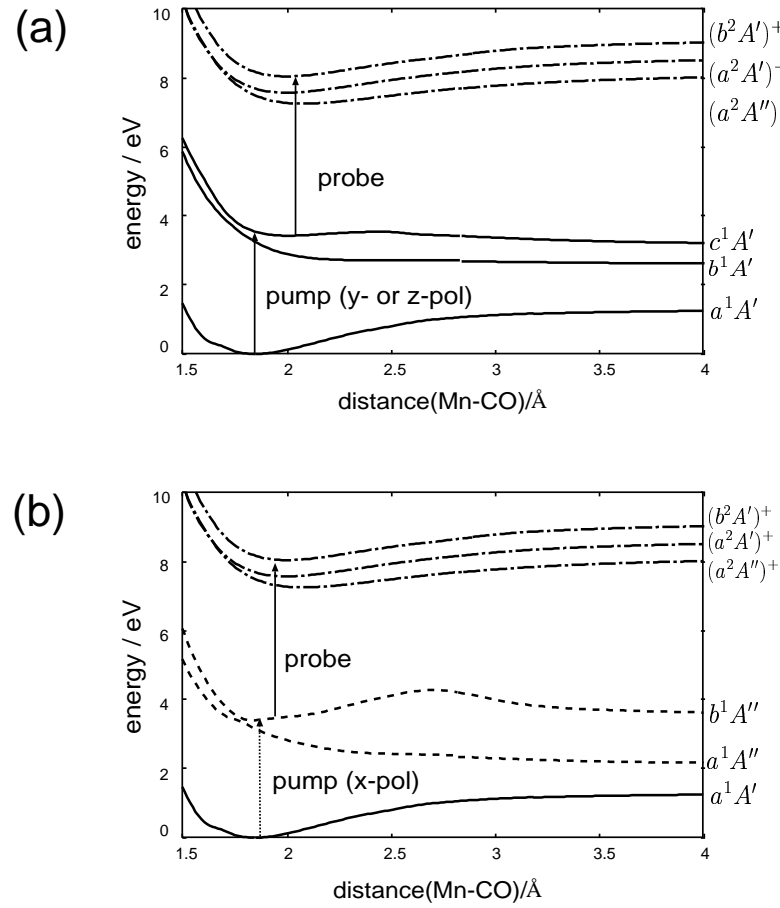


Figure 4.1: The two excitation (pump) processes investigated in this section and in section 4.5: Panel (a) : The $c^1 A'$ state is populated by z- (and less efficiently by y-) polarized light. Panel (b): The $b^1 A''$ is populated by x-polarized light. The ionic states are equally populated by the probe pulse using arbitrary polarizations.

ture (see chapter 2):

$$\left(\begin{array}{ccccccc} & a^1 A' & a^1 A'' / b^1 A' & b^1 A'' / c^1 A' & (a^2 A'')^+ & (a^2 A')^+ & (b^2 A')^+ \\ a^1 A' & \dots & \dots & \dots & \dots & \dots & \dots \\ a^1 A'' / b^1 A' & \dots & \dots & \dots & \dots & \dots & \dots \\ b^1 A'' / c^1 A' & \dots & \dots & \dots & \dots & \dots & \dots \\ (a^2 A'')^+ & \dots & \dots & \dots & \dots & \dots & \dots \\ (a^2 A')^+ & \dots & \dots & \dots & \dots & \dots & \dots \\ (b^2 A')^+ & \dots & \dots & \dots & \dots & \dots & \dots \end{array} \right).$$

To study the influence of the $b^1 A' - c^1 A'$ coupling, the $c^1 A'$ state is populated using a z-polarized laser (a y-polarized laser is less efficient because of the smaller transition dipole moment (TDM) (see section 3.5)) with $\epsilon_x^0 = 0.5$ GV/m, $t^{pulse} = 100$ fs (37 fs in Full Width at Half Maximum (FWHM)) of the intensity and the

(adiabatic) resonant frequency, $\hbar\omega = 3.55$ eV. The $a^1A'' - b^1A''$ population transfer is observed after exciting the b^1A'' state by an x-polarized laser with an (adiabatic) resonant frequency, $\hbar\omega = 3.40$ eV and the same ϵ_x^0 and t^{pulse} values. Note that in the diabatic picture the adiabatic resonant frequencies are off-resonant promoting less population to the excited states. Nevertheless, the same (adiabatic) "pump" frequencies have been used in both representations. The electric field strength ($\epsilon_x^0 = 0.5$ GV/m) has been chosen such that less than 10% population is electronically excited in order to prevent the subsequent (probe) pulse from inducing unphysical back-transformation (dump) of ionic state population (*cf* section 2.5). According to equation (4.2),

$$I_{max} = \varepsilon_0 \cdot c \cdot (\epsilon^0)^2, \quad (4.2)$$

where ε_0 is the vacuum permittivity and c is the speed of light, the maximum intensity I_{max} corresponds to $0.07 \cdot 10^{12}$ W/cm² [127].

Recall that to calculate the transformation matrix that connects the adiabatic with the diabatic picture, equation (2.37) must be solved using the kinetic coupling matrix $\underline{\underline{T}}^{(1)}$. The kinetic coupling terms $T^{(1)}$ and $T^{(2)}$ were depicted in figures 3.8, 3.10, 3.11 and 3.12. Since the applied laser frequencies only populate significantly the b^1A' , c^1A' , a^1A'' , and b^1A'' states, the couplings among the other states (see section 3.5) can be neglected and the transformation matrix simplifies to:

$$\underline{U} = \begin{pmatrix} 1 & 0 & 0 & 0 & 0 & 0 \\ 0 & U_{22} & U_{23} & 0 & 0 & 0 \\ 0 & U_{32} & U_{33} & 0 & 0 & 0 \\ 0 & 0 & 0 & 1 & 0 & 0 \\ 0 & 0 & 0 & 0 & 1 & 0 \\ 0 & 0 & 0 & 0 & 0 & 1 \end{pmatrix}. \quad (4.3)$$

This matrix implies that only the b and c diabatic states of A' symmetry and the a and b states of A'' symmetry are different from the corresponding adiabatic states, whereas the other states remain the same under the unitary transformation (4.3). To determine the matrix \underline{U} the algorithm described in ref. [61] was used. The resulting diabatic potentials with the corresponding potential couplings are shown in figure 4.2 and figure 4.3 for the states of A' and A'' symmetry, respectively. In each symmetry there are crossings occurring at 1.70 Å and 1.78 Å for the A' and A'' states, respectively.

Applying the transformation (4.3) on the dipole matrix yields the diabatic transition dipole moments depicted in figure 4.4.

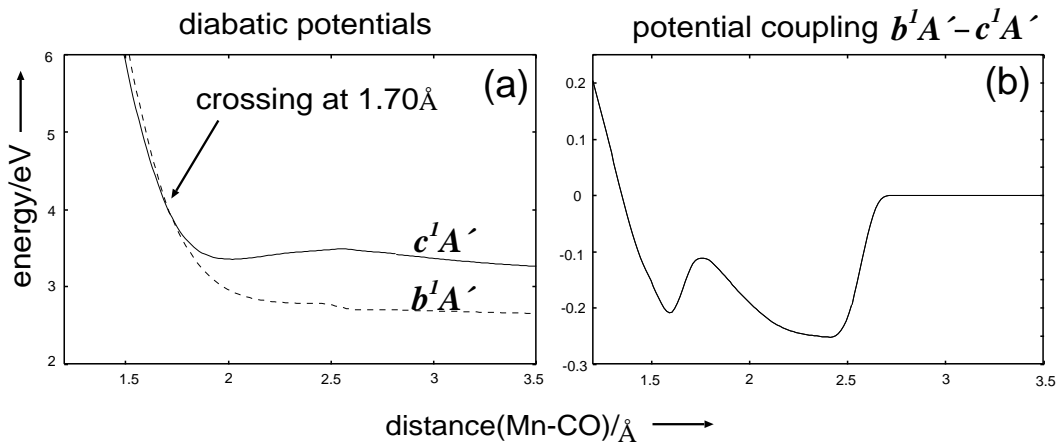


Figure 4.2: (a) Diabatic potentials b^1A' and c^1A' . (b) $b^1A' - c^1A'$ potential coupling.

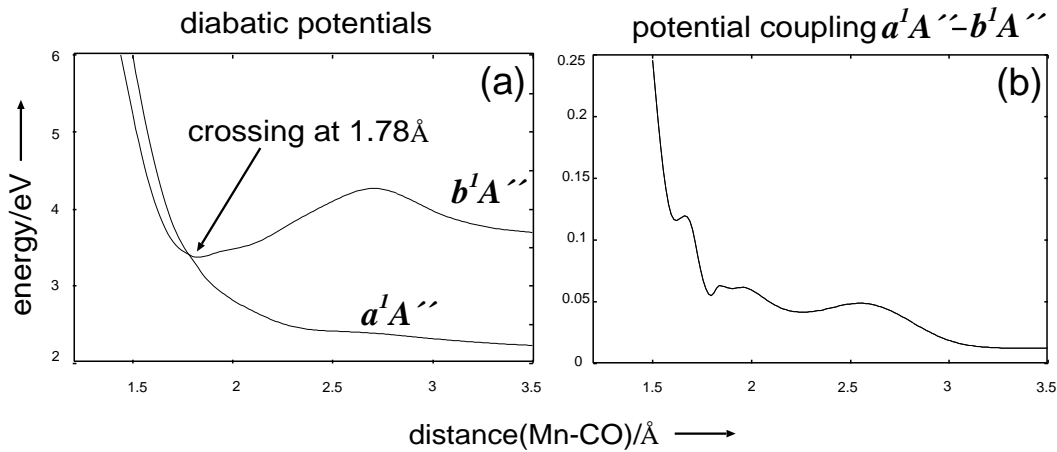


Figure 4.3: (a) Diabatic potentials a^1A'' and b^1A'' . (b) $a^1A'' - b^1A''$ potential coupling.

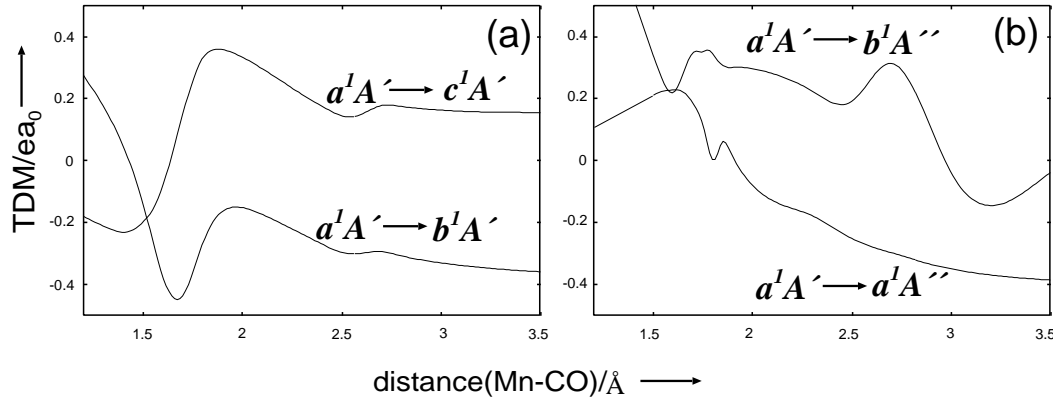


Figure 4.4: Diabatic transition dipole moments (a) $a^1A' \rightarrow b^1A' / c^1A'$, (b) $a^1A' \rightarrow a^1A'' / b^1A''$.

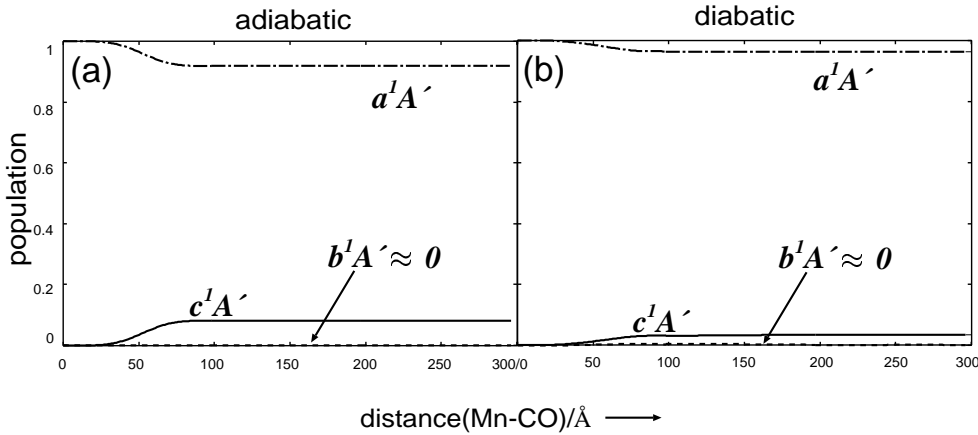


Figure 4.5: Influence of the $b^1A' - c^1A'$ kinetic coupling on the population dynamics of the states c^1A' (solid line), b^1A' (dashed line) and a^1A' (dot-dashed line) after a \sin^2 -pulse of 100 fs duration. (a) Adiabatic representation including kinetic coupling. (b) Diabatic representation including potential coupling.

The simulations shown in figure 4.5 demonstrate that the diabatic coupling between the b^1A' and c^1A' states induces a marginal population transfer, independent of the adiabatic or diabatic picture. The overall population transfer to the excited states is however smaller in the diabatic representation due to the slightly off-resonant excitation energies ($E_{c^1A'}^{dia} - E_{a^1A'}^{ida} \approx 3.47$ eV, $E_{b^1A''}^{dia} - E_{a^1A'}^{dia} \approx 3.38$ eV, at $q_a^{Franck-Condon} \approx 1.85$ Å). Even five times higher $T^{(1)}$ and $T^{(2)}$ coupling terms do not increase the transfer of population to the dissociative states such that the pump-probe spectrum is affected. As a consequence, the $b^1A' - c^1A'$ coupling has been safely neglected in the coming theoretical simulations.

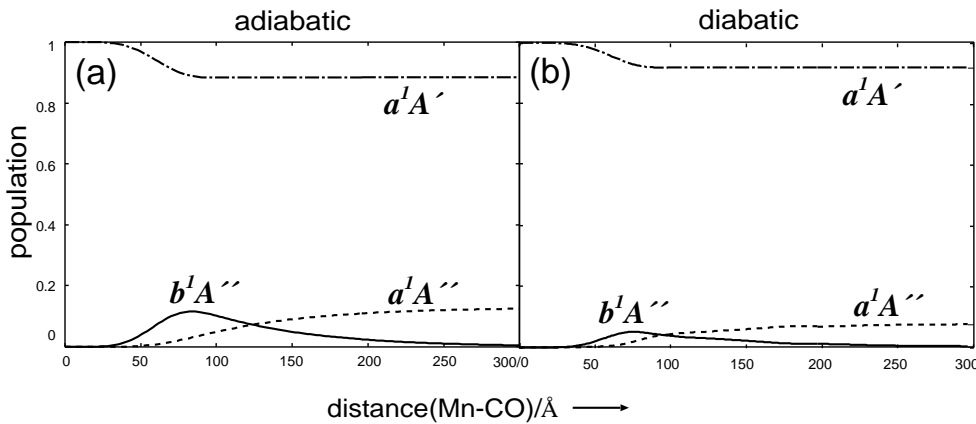


Figure 4.6: Influence of the $a^1A'' - b^1A''$ coupling on the population dynamics of the states b^1A'' (solid line), a^1A'' (dashed line) and a^1A' (dot-dashed line) after a \sin^2 -pump pulse of 100 fs duration. (a) Adiabatic representation including kinetic coupling. (b) Diabatic representation including potential coupling.

Compared with the $b^1A' - c^1A'$ coupling, the maximum of the $a^1A'' - b^1A''$ coupling (cf figures 3.10 and 3.12) is shifted more toward the Franck-Condon point ($q_a^{Franck-Condon} \approx 1.85 \text{ \AA}$) and a stronger effect upon the dynamics can be anticipated. This shift is reflected in the diabatic picture since the crossing of the A' states is located at 1.70 \AA whereas that of the A'' states appears at 1.78 \AA . The dynamical simulations shown in figure 4.6 confirm this hypothesis.

An x-polarized pump pulse with the adiabatic resonant frequency, $\hbar\omega = 3.40 \text{ eV}$, populates predominantly the b^1A'' state which reaches the maximum amount of population at about 80 fs (pulse duration = 100 fs). Due to the nonadiabatic coupling the population of the b^1A'' state starts rising at 50 fs and at 300 fs practically all the population is transferred from the b^1A'' to the a^1A'' state. Despite the fact that the diabatic states are less populated than the corresponding adiabatic ones (because the $a^1A' \rightarrow b^1A''$ excitation is off-resonant by 0.02 eV), the adiabatic and diabatic representations yield, as expected, equivalent results. Therefore, from now on only the adiabatic representation will be employed since its interpretation (especially of the transition energies) is straightforward (see section 2.2.4).

4.2 Theoretical absorption spectrum

The absorption spectrum has been calculated according to equation (2.71) with and without (for the sake of comparison) the $a^1A'' - b^1A''$ kinetic couplings. Again, only the four lowest low-lying electronic excited states, b^1A' , c^1A' , a^1A'' , b^1A'' , have been included since for these states the MR-CCI method closely resembles the MS-CASPT2 results. Indeed, the deviations do not exceed 0.2 eV (*cf* table 3.5). Furthermore, they are accessible within the energy domain of the experimental pulses ($\approx 400\text{nm} (=3.10\text{ eV})$) and - as mentioned in section 3.4 - contribute to the first band of the experimental absorption spectrum.

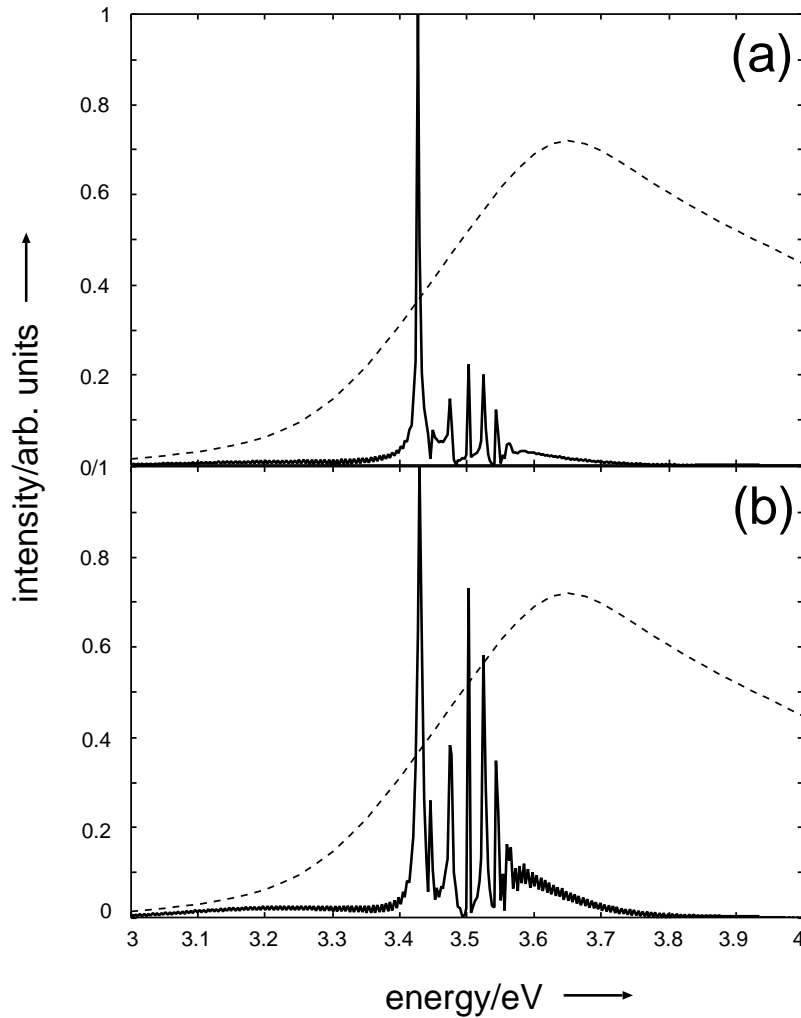


Figure 4.7: Theoretical gas phase (solid lines) and experimental liquid phase [46] (dashed lines) electronic absorption spectra for $\text{CpMn}(\text{CO})_3$. Panel (a): Theoretical spectrum without $a^1A'' - b^1A''$ kinetic coupling. Panel (b): Theoretical spectrum with $a^1A'' - b^1A''$ kinetic coupling.

The theoretical spectrum has been obtained by propagation of the starting one-

dimensional excited state wavepackets, which have been calculated as the electronic and vibrational ground state Θ_{0_0} scaled by the absolute value of the transition dipole moments μ_{i0} at the Franck-Condon point ($q_a^{Franck-Condon} \approx 1.85 \text{ \AA}$) for each transition, normalized in the following way (for details, see appendix A):

$$\bar{\mu}_{i0} = \frac{\sqrt{\mu_{i0,x}^2 + \mu_{i0,y}^2 + \mu_{i0,z}^2}}{\sqrt{\sum \mu_{i0}^2}} \quad (4.4)$$

This results in the following initial conditions:

$$\chi_{b^1A'}(q_a, t = 0) = 0.450 \cdot \Theta_{0_0}(q_a)$$

$$\chi_{c^1A'}(q_a, t = 0) = 0.705 \cdot \Theta_{0_0}(q_a)$$

$$\chi_{a^1A''}(q_a, t = 0) = 0.027 \cdot \Theta_{0_0}(q_a)$$

$$\chi_{b^1A''}(q_a, t = 0) = 0.547 \cdot \Theta_{0_0}(q_a) \quad (4.5)$$

The theoretical simulation concentrates on the first band of the experimental spectrum (in solution), which extends from 3.10 eV (400 nm) till 4.3 eV (290 nm) with a maximum at 3.65 eV (240 nm) [46]. This band is shown in figure 4.7 together with the theoretical results. Solvent-effects which might lead to a red-shift [128] should not play a role since an unpolar solvent, isoctane, has been used in the present case [46]. Neglecting the $a^1A'' - b^1A''$ kinetic couplings, the theoretical spectrum shows an intense narrow peak at 3.40 eV, which is normalized to unity (figure 4.7 (a)). This peak corresponds to the bound state b^1A'' which has a minimum at nearly the same position as the electronic ground state ($q_a^{Franck-Condon} \approx 1.85 \text{ \AA}$) leading to a large Frank-Condon factor. This narrow peak at 3.40 eV expresses the dominant contribution of a single eigenstate (the vibrational ground state of b^1A''), whose density and corresponding autocorrelation function does not change with time. As expected, it becomes broader when the $a^1A'' - b^1A''$ coupling is taken into account. Consequently, the following peaks at around 3.55 eV are much more pronounced in the coupled case (figure 4.7 (b)). These peaks indicate a superposition of vibrational eigenstates propagated on the c^1A' potential. The dissociative state b^1A' shows a weak, broad band around 3.2 eV and the a^1A' state does not contribute to the spectrum due to its low TDM.

In conclusion, the main features of the lowest part of the absorption spectrum (between 3.2 and 3.6 eV) of $\text{CpMn}(\text{CO})_3$ have been reproduced in the limit of a one-dimensional approach.

4.3 Probability of dissociation on the b^1A' and c^1A' states using rotational averaging

As described in section 2.3 a probability of dissociation can be calculated using time-dependent excited states wave packets. As a first guess this has been done on the two lowest-lying excited states of A' symmetry, b^1A' and c^1A' , where the nonadiabatic coupling can be safely neglected (see section 4.1) *i.e.* the dynamics is governed by equation (2.48) (Born-Oppenheimer dynamics). This means that the rotational averaging is performed only over the y- and z-polarized lasers neglecting the x-component.

A different labeling of the electronic states is used here, namely the a^1A' is denoted by X and the b^1A' and c^1A' states are labeled B and C, respectively.

There are four cases to be studied, namely δ -pulse excitations with y- or z-polarized light to the B (b^1A') and C (c^1A') states. The dissociation probability of these four cases is calculated according to equation (2.59). A somewhat arbit-

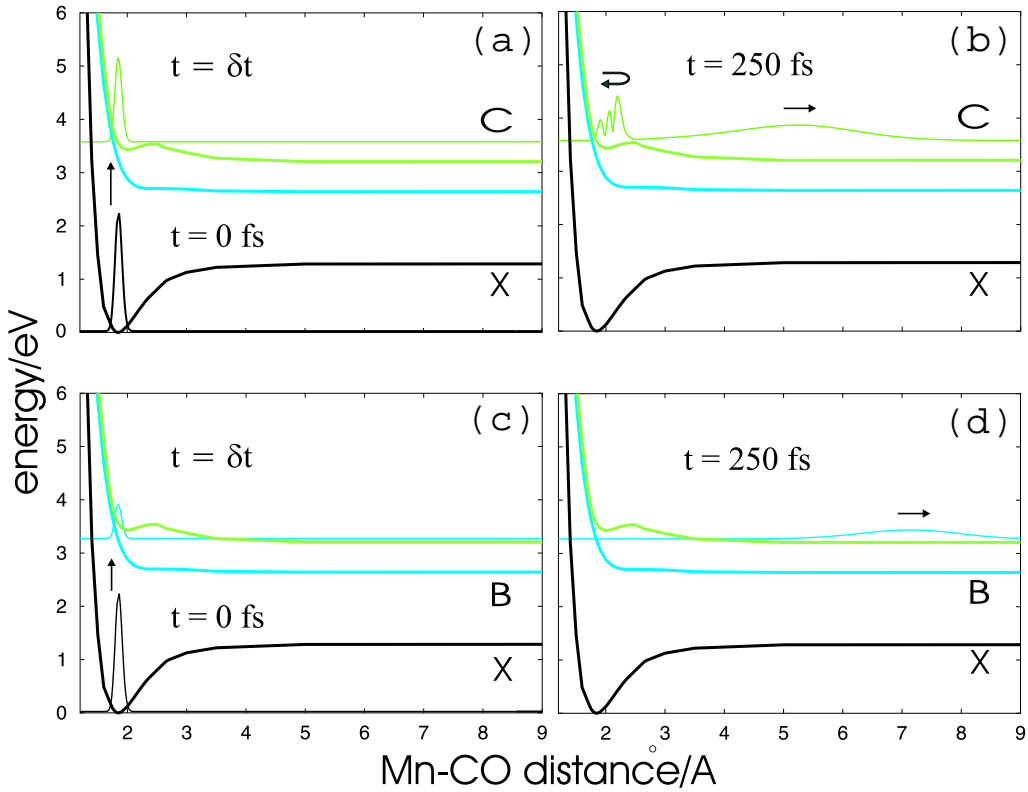


Figure 4.8: *Born-Oppenheimer dynamics of the laser- δ -pulse driven wave packet of $CpMn(CO)_3$ on CASSCF/MR-CCI, B and C, potentials. Panels (a) and (b): snapshots on the potential c^1A' (C) for $t=0$, δt and $t = 250$ fs, respectively. Panels (c) and (d) on the potential b^1A' (B) for $t=0$, δt and $t = 250$ fs, respectively.*

rary, yet reasonable choice of b in equation (2.59), on the basis of molecular orbitals, is $b=5.4 \text{ \AA}$ (\approx three times the equilibrium distance of the X potential). Hence, the total dissociation probability is the sum of the resulting four probabilities of dissociation weighted by a factor that takes into account the different strengths of the transition dipole moments. As weighting factors the norm of the initial wave function multiplied by the corresponding transition dipole moment functions were employed:

$$w_i = \frac{\sum_{n=1}^N (\mu_{i0,y/z}(n) \cdot \Theta_{00}(n))^2}{\sum_i \sum_{n=1}^N (\mu_{i0,y/z}(n) \cdot \Theta_{00}(n))^2}, \quad (4.6)$$

where n denotes the grid point and N is the total number of grid points. The resulting weights calculated according to (4.6) are:

$$w_{By} = 0.28, \quad w_{Bz} = 0.01, \quad w_{Cy} = 0.01 \text{ and } w_{Cz} = 0.70, \quad (4.7)$$

where the index "By/z" denotes the X (a^1A') \rightarrow B (b^1A') and "Cy/z" the X (a^1A') \rightarrow C (c^1A') transition using y- or z-polarized light. Finally, the total dissociation probability $\overline{P_{diss}(t)}$ is the sum of the individual dissociation probabilities multiplied by the corresponding weighting coefficient:

$$\overline{P_{diss}(t)} = 0.28 \cdot P_{diss,By}(t) + 0.01 \cdot P_{diss,Bz}(t) + 0.01 \cdot P_{diss,Cy}(t) + 0.70 \cdot P_{diss,Cz}(t). \quad (4.8)$$

Note that the calculation of $\overline{P_{diss}(t)}$ according to equation (4.8) implies a rotational averaging described in section 2.3 (cf equations (2.69) and (2.70)).

For a comparison with the experimental result which does not resolve these individual contributions, the expression (4.8) is fitted to an exponential rise time of products in the asymptotic time domain,

$$\frac{\overline{P_{diss}(t)}}{\overline{P_{diss}}} \propto 1 - \exp[(t - t_b)/\tau], \quad (4.9)$$

where $\overline{P_{diss}}$ is the asymptotic ($t = t_{as}$) dissociation probability, and t_b is an irrelevant time delay depending on, and compensating for somewhat arbitrary, albeit reasonable choices of the boundary b (for example, $t_b = 250 \text{ fs}$ for $b = 5.4 \text{ \AA}$). In practice, one determines:

$$\overline{P_{diss}} \approx \overline{P_{diss}}(t_{as}), \quad (4.10)$$

where t_{as} is sufficiently large so that $\overline{P_{diss}(t)}$ does not increase significantly for times t beyond t_{as} ; in the present case, $t_{as} = 450 \text{ fs}$ is used.

The relevant potentials, X (a^1A'), B (b^1A') and C (c^1A'), are depicted in figure 4.8 together with snapshots of the wave packets at different times ($t = 0, \delta t, 250$

fs). Specifically, each of the wavepackets $\chi_i(t)$ is represented by the corresponding probability density $\rho_i(t) = |\chi_i(t)|^2$ embedded in the relevant potential V_i , with a base line indicating the average total energy:

$$E_i = \frac{\langle \chi_i | T + V_i | \chi_i \rangle}{\langle \chi_i | \chi_i \rangle}. \quad (4.11)$$

In particular, figure 4.8 shows the initial ($t=0$) wavepacket Θ_{00} embedded in V_0 , as well as the wavepackets (at $t=\delta t$), $\chi_{By} = \mu_{By} \cdot \Theta_{00}$ and $\chi_{Cz} = \mu_{Cz} \cdot \Theta_{00}$, with proper renormalization. Obviously, the δ -pulse induces more efficient excitations to the C ($c^1 A'$) potential in comparison with the B ($b^1 A'$) potential, in accord with the values of the transition dipole moments in the Franck-Condon region, *cf* figure 3.4. As already pointed out in section 3.5, the absolute values of the y and z components are quite different in the Franck-Condon region. For that reason, one obtains the y-component for the X ($a^1 A'$) \rightarrow B ($b^1 A'$) transition about $0.28 \text{ } ea_0$ whereas the y-component for the X ($a^1 A'$) \rightarrow C ($c^1 A'$) excitation is approximately zero. On the contrary the z-component is large for the X ($a^1 A'$) \rightarrow C ($c^1 A'$) transition ($0.42 \text{ } ea_0$) and practically vanishes for the X ($a^1 A'$) \rightarrow B ($b^1 A'$) excitation.

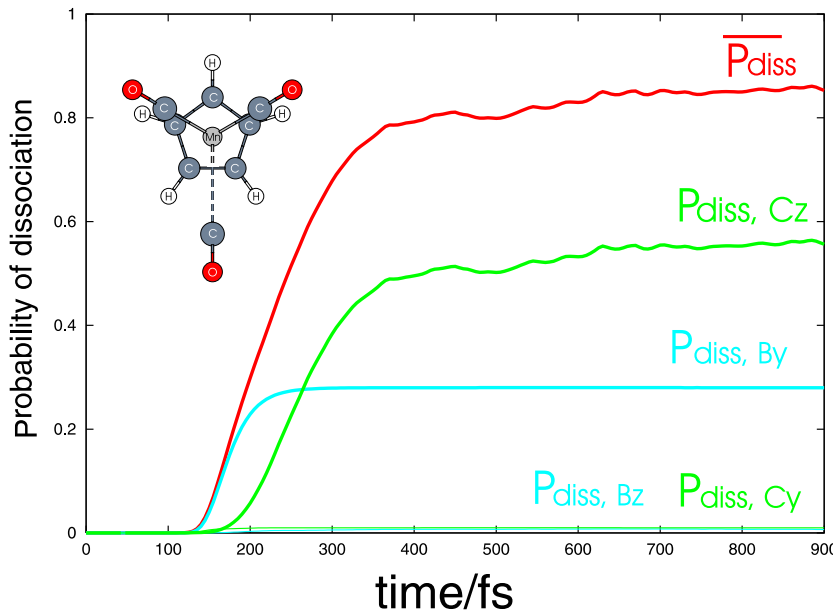


Figure 4.9: Overall orientationally averaged probability \overline{P}_{diss} and its four contributions, $P_{diss,Cz}$, $P_{diss,By}$, $P_{diss,Bz}$ and $P_{diss,Cy}$.

The snapshots of the molecular wavepackets at $t=250$ fs presented in figure 4.8 demonstrate direct and nearly complete dissociation of χ_{By} on the strongly repulsive potential B ($b^1 A'$). In contrast, the potential barrier of the C ($c^1 A'$) state causes the separation of χ_{Cz} into two partial waves: one of them represents the fraction of χ_{Cz} which is essentially trapped in the local well of the potential C ($c^1 A'$) close to

the Frank-Condon window, whereas the other one represents the complementary fraction of χ_{Cz} which dissociates, albeit slower than χ_{By} , due to the less repulsive slope of the potential C ($c^1 A'$), for $q_a \approx q_a^{Frank-Condon}$, in comparison with B ($b^1 A'$).

The resulting probabilities of dissociation are shown in figure 4.9. Accordingly, the orientationally averaged overall dissociation probability, $\overline{P}_{diss}(t)$, consists of two significant contributions, $P_{diss,By}(t)$ and $P_{diss,Cz}(t)$, whereas the complementary terms, $P_{diss,Bz}(t)$ and $P_{diss,Cy}(t)$, are negligible. As aforeindicated this is due to the different weights of the underlying wavepackets (cf equation (4.7)). Comparison of figure 4.8 and 4.9 reveals that the dominant component $P_{diss,Cz}(t)$ arises from the relatively slow dissociation of χ_{Cz} on the potential C ($c^1 A'$), whereas the smaller component $P_{diss,By}(t)$ is due to the faster dissociation of χ_{By} on B ($b^1 A'$). The fit of the averaged theoretical dissociative lifetime, τ , (cf equation 4.9), is, therefore, dominated by $P_{diss,Cz}(t)$. We have checked that the value of τ does not depend significantly on the choice of the boundary b , within reasonable values from 5 to 7 Å.

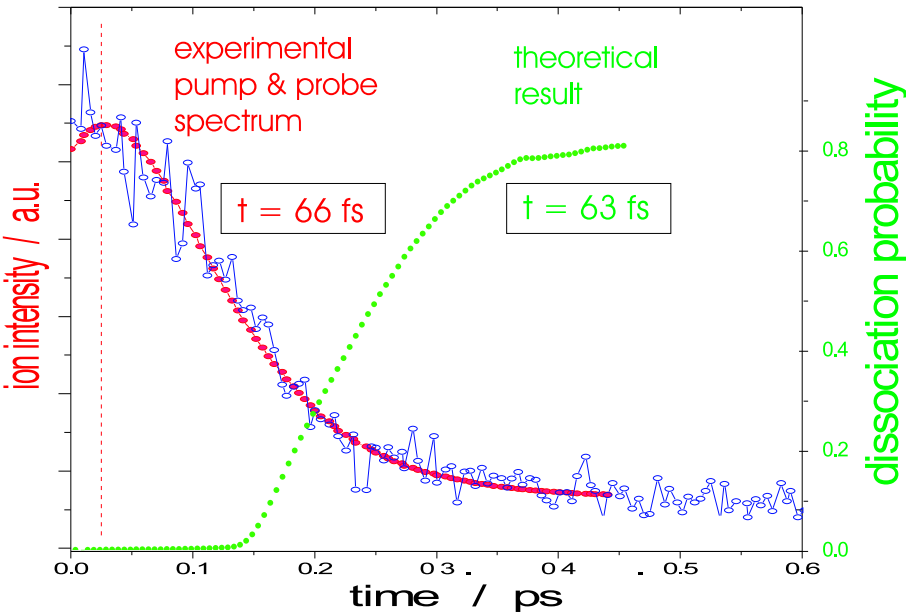


Figure 4.10: Comparison of the experimental dissociative lifetime ($t=66$ fs) with the theoretical exponential rise time of the products ($\tau=63$ fs), (cf eq. (4.9)).

In a previous paper [24] the theoretical decay of the pump-probe signal for the loss of the first CO ligand, $\tau = 66$ fs, has been compared with our theoretical exponential rise time of the products, $\tau = 63$ fs (cf figure 4.10). Both, the experimental decay as well as the theoretical rise time indicate that the photodissociation of $CpMn(CO)_3$ takes place on a 100 fs time scale. This is an important result for our further investigations. \sin^2 -shaped laser pulses (equation 4.1) are used to sim-

ulate the effects of the pump (section 4.4) and the pump followed by a probe (section 4.5).

4.4 Dynamics on the low-lying excited states potentials induced by femtosecond laser pulses

As already pointed out in previous sections, the transition dipole moments corresponding to the A' states possess two components, y or z , (the x -component vanishes for symmetry reasons). As a consequence, the initial wavepacket can be photoexcited using y - or z -linearly polarized laser pulses. In contrast, the A'' states are photoexcited using x -polarized laser pulses. All transition dipole moments are shown in figure 3.4 for the x -, y - and z -components.

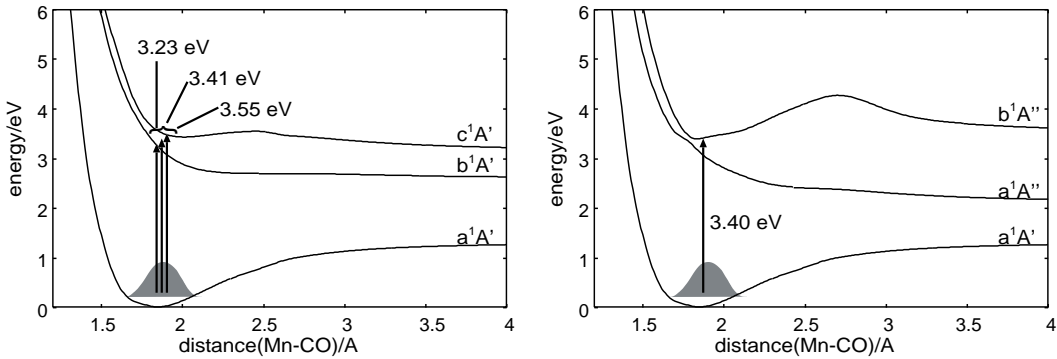


Figure 4.11: *Applied laser pulses in the case of the A' and A'' potential energy curves: 3.23 eV (resonant with $b^1 A'$), 3.55 eV (resonant with $c^1 A'$), 3.41 eV (average of 3.23 eV and 3.55 eV) and 3.40 eV (resonant with $b^1 A''$) (the resonant energy of the $a^1 A''$ is not investigated (see text)).*

In this section we chose laser parameters close to the experimental ones: $\epsilon_{y/z}^0 = 5.5 \text{ GV/m}$ equivalent to an intensity $I_{max} \approx 8.0 \cdot 10^{12} \text{ W/cm}^2$ for the A' states and $\epsilon_x^0 = 1.0 \text{ GV/m}$ equivalent to $I_{max} = 0.3 \cdot 10^{12} \text{ W/cm}^2$ for the A'' states. In both cases a pulse duration of $t_{pulse} = 100 \text{ fs}$ equivalent to ca. 37 fs for FWHM in intensity was applied. The molecule was excited with three different energies $\hbar\omega = 3.23 \text{ eV}$, 3.55 eV and 3.41 eV , for simulations on the A' potentials, and a single frequency, $\hbar\omega = 3.40 \text{ eV}$, in the case of simulations on A'' curves. These frequencies correspond to the (adiabatic) resonant Franck-Condon $a^1 A' \rightarrow b^1 A'$, $a^1 A' \rightarrow c^1 A'$ transitions, to some intermediate value bringing the molecular system between the $b^1 A'$ and $c^1 A'$ states, and to the resonant Franck-Condon $a^1 A' \rightarrow b^1 A''$ transition, respectively, all of them illustrated in figure 4.11.

As seen in figure 3.4 the transition dipole moments connecting the a^1A' and the a^1A'' is very small. Test calculations using a laser frequency resonant to the a^1A'' state, $\hbar\omega = 3.13$ eV, (with intensities and pulse lengths given above) yield a marginal population transfer to the a^1A'' state. Therefore, simulations with $\hbar\omega = 3.13$ eV are not considered. As in the calculation of the absorption spectrum in section 4.2 only the $a^1A'' - b^1A''$ kinetic coupling has been taken into account.

The molecule is assumed to be non-rotating and it is photoexcited either with y- or with z-linearly polarized light when excited to the A' states and with linearly polarized light in the x direction if excited to states of A'' symmetry. Due to the very different behaviour of the transition dipole moments around the Franck-Condon window the amount of population that will be transferred from the ground state to some excited state will depend very much on which component of the transition dipole moment is used (figure 3.4). Within the states of interest, b^1A' and c^1A' , the z-component for the $a^1A' \rightarrow b^1A'$ excitation and the y-component for the $a^1A' \rightarrow c^1A'$ excitation are approximately zero. Therefore, significant amount of population (within reasonable laser intensity) will be transferred to the b^1A' when using y-polarized light and the resonant energy of b^1A' , $\hbar\omega = 3.23$ eV, whereas the c^1A' will be mainly populated if z-polarized light and the resonant energy of c^1A' , $\hbar\omega = 3.55$ eV, is used. Indeed, for the aforementioned transitions the complementary z- and y-pulses, *i.e.* a y-polarized laser with energy $\hbar\omega = 3.55$ eV or a z-polarized laser with energy $\hbar\omega = 3.23$ eV, induce less than 10 % population inversion with the present intensity.

The resulting population dynamics and wavepacket evolution on the three relevant states, a^1A' , b^1A' and c^1A' , for $\hbar\omega = 3.23$ eV and 3.55 eV are shown in figures 4.12 and 4.13, respectively. As shown in figure 4.12(a) the use of ϵ_y together with the y component of the transition dipole moment and a laser energy of 3.23eV results in ca. 70 % population inversion from the electronic and vibrational ground state to b^1A' . The laser is intense enough as to return population to the ground state by stimulated emission, as indicated by the residual population in the ground state vibrational level $v=1$. Figure 4.12(c) demonstrates direct dissociation as expected from a repulsive state. In contrast, using ϵ_z and the z component of the transition dipole moment a laser pulse of energy of 3.55 eV populates in about the same amount the c^1A' state. Likewise, small populations of the ground state with $v = 1$ and $v = 2$ indicate stimulated emission (see figure 4.13(a)). The wavepacket simulations depicted in figures 4.13(b) and 4.13(c) indicate that the marginal population of the b^1A' state runs away as fast as when using 3.23 eV, cf. figure 4.12(c). On the contrary, the wave packet on the c^1A' potential splits into two partial waves due to the small energy barrier at 2.5 Å. The main part remains trapped and oscillates in the potential well, whereas another fraction overcomes the small barrier

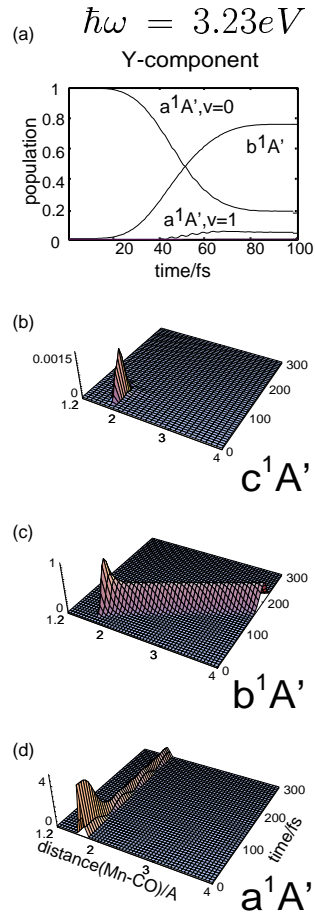


Figure 4.12: Adiabatic time evolution of the laser driven simulations on $\text{CpMn}(\text{CO})_3$ under y -linearly polarized light of $\hbar\omega = 3.23 \text{ eV}$ (frequency resonant with b^1A' state) and $t_{\text{pulse}} = 100 \text{ fs}$. Panel (a) shows the time evolution of the population dynamics, as defined in section 2.2.6. Panels (b), (c) and (d) show the time evolution of the wavepacket on the c^1A' , b^1A' and a^1A' states, respectively.

(0.2 eV) and dissociates, although slower than in the b^1A' state. These results are in agreement with the simulations performed using a δ -pulse described in section 4.3.

When an intermediate energy $\hbar\omega = 3.41 \text{ eV}$ is used, about half of the population is transferred to either the b^1A' or to the c^1A' states, depending on whether y - or z -polarized pulses are employed, respectively. The results are shown in figure 4.14 for y - and z - pulses. The y -polarized pulse transfers preferentially population from a^1A' to b^1A' and as it happened in the case shown in figure 4.12(c) it dissociates rapidly on the repulsive state, see *l.h.s* of figure 4.14(a) and (c).

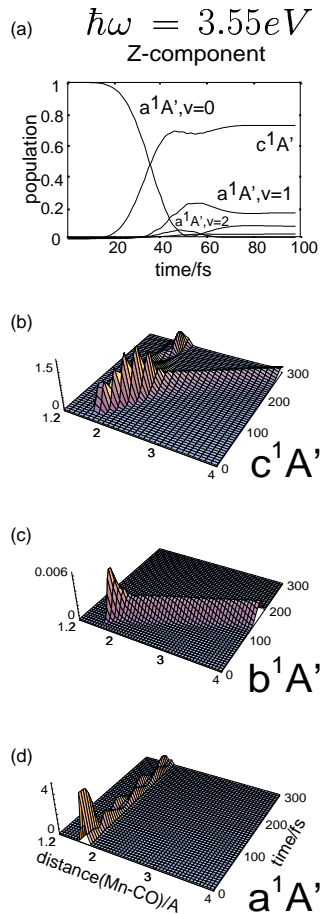


Figure 4.13: Adiabatic time evolution of the laser driven simulations on $\text{CpMn}(\text{CO})_3$ under z-linearly polarized light of $\hbar\omega = 3.55 \text{ eV}$ (frequency resonant with $c^1 \text{A}'$ state) and $t_{\text{pulse}} = 100 \text{ fs}$. Panel (a) shows the time evolution of the population dynamics. Panels (b), (c) and (d) show the time evolution of the wave-packet on the $c^1 \text{A}'$, $b^1 \text{A}'$ and $a^1 \text{A}'$ states, respectively.

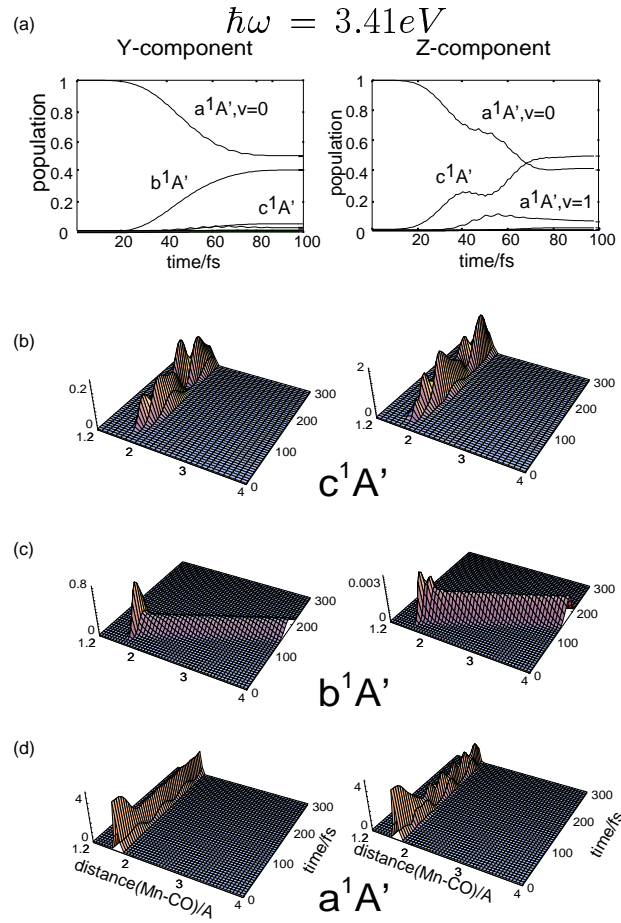


Figure 4.14: Adiabatic time evolution of the laser driven simulations on $CpMn(CO)_3$ under y - and z -linearly polarized light of $\hbar\omega = 3.41 \text{ eV}$ (averaged frequency between the $b^1 A'$ and $c^1 A'$ state) and $t_{pulse} = 100 \text{ fs}$. Panel (a) shows the time evolution of the population dynamics. Panels (b), (c) and (d) show the time evolution of the wavepacket on the $c^1 A'$, $b^1 A'$ and $a^1 A'$ states, respectively.

The residual population which reaches the $c^1 A'$ state is trapped in the local well (figure 4.14(b)). The same effects can be observed if a z -polarized laser pulse is used. Half of the population is inverted from the $a^1 A'$ to the $c^1 A'$ state and it remains completely trapped in the local well and oscillates with a full period of about 150 fs (depending on the excitation energy), as depicted in the r.h.s. of figure 4.14(b). Also apparent is that the wavepacket located in the $a^1 A'$ potential exchanges amplitude during the laser pulse as demonstrated in the population dynamics of figure 4.14(a). The population of the $c^1 A'$ state clearly reveals a loss of amplitude when the pulse reaches its maximum of intensity, which is transferred to the ground state with $v = 1$, indicating an intra-pulse-pump-dump process.

Next, let us consider the selective preparation of cymantrene in the excited A''

states. For this purpose the x-component of the transition dipole moment is used. As seen in figure 3.4, the value for the $a^1A' \rightarrow a^1A''$ transition at the Franck-Condon region is close to zero, and therefore transitions to this state would require a very intense laser pulse, in comparison to the intensity needed to reach other accessible states, as i.e. b^1A'' . Note that the oscillator strength of this state reported in section 3.5 at CASSCF level was predicted to be of the same order of magnitude as for the $a^1A' \rightarrow a^1A''$ transition, and zero at TD-DFT level. The discrepancy between the previous CASSCF results and the present ones comes from the slight shift of the a^1A' potential minimum on going from CASSCF to MR-CCI level (from 1.81 Å to 1.85 Å at MR-CCI level). Thus, only simulations on the b^1A'' (fig. 4.15) state will be shown.

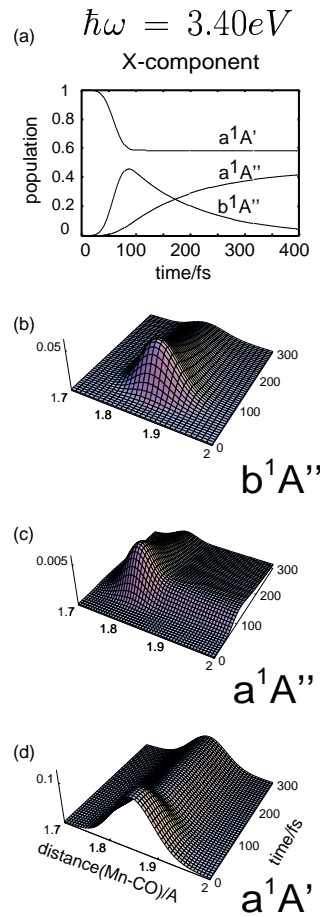


Figure 4.15: Adiabatic time evolution of the laser driven simulations on $\text{CpMn}(\text{CO})_3$ under x-linearly polarized light of $\hbar\omega = 3.40$ eV (frequency resonant with b^1A'' state) and $t_{\text{pulse}} = 100$ fs. Panel (a) shows the time evolution of the population dynamics. Panels (b), (c) and (d) show the time evolution of the wavepacket on the b^1A'' , a^1A'' and a^1A' states, respectively.

As discussed in section 4.1 the diabatic coupling connecting the b^1A' with the c^1A' is negligible but the coupling between the a and b states of symmetry A'' has a strong influence on the dynamics. The population dynamics using a laser with an electric field of 0.5 GV/m has already been discussed there. An electric field of 1.0 GV/m is enough to invert ca. 50 % of the population from the electronic and vibrational ground state a^1A' to the b^1A'' state, as shown in figure 4.15(a), since the value of the transition dipole moment for the $a^1A' \rightarrow b^1A''$ transition does not decay outside of the Franck-Condon window as quickly as in the case of A' transitions. The wave packet is trapped in the b^1A'' state due to its bound character and a maximum of population in this state is reached at around 80 fs. The population reaching the state a^1A'' by the $a^1A'' - b^1A''$ kinetic coupling dissociates directly, cf figure 4.15(b) and (c), respectively. Note that population trapped in the b^1A'' state does not apparently oscillate for the minimum position matches very much the one of the electronic ground state, a^1A' .

In summary these simulations illustrate that, different products could be observed in the probe state depending on where the wavepacket is prepared. If the initial pump pulse prepares a state completely localized in the weakly bound c^1A' state (figure 4.14) no dissociation should occur and only a signal for the parent ion, $\text{CpMn}(\text{CO})_3^+$, should be observed after the probe pulse. In contrast, if the pump frequency is such that the wave packet has enough kinetic energy to overcome the barrier in the c^1A' state (figure 4.13), or if it selects the repulsive b^1A' state (figure 4.12) or reaches the repulsive a^1A'' state via the $a^1A'' - b^1A''$ coupling (figure 4.15), it will undergo fast dissociation and the probe pulse would detect the fragment $\text{CpMn}(\text{CO})_2^+$. These statements assume non-rotating molecules and specific polarizations. Obviously in the case of free rotating molecules all components of the laser pulse would interact at the same time. However, in the present case the transition dipole moments, which govern the electronic populations, are characterized by a single dominant component which is non zero, and consequently the computer simulations are still valid.

4.5 Simulation of pump-probe and control experiments

In this section the excited state dynamic which has been analyzed carefully in the previous sections is probed by a second laser pulse that ionizes the molecule.

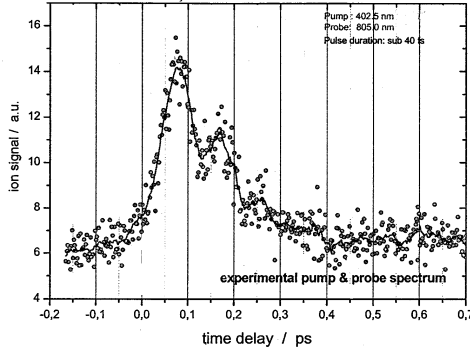
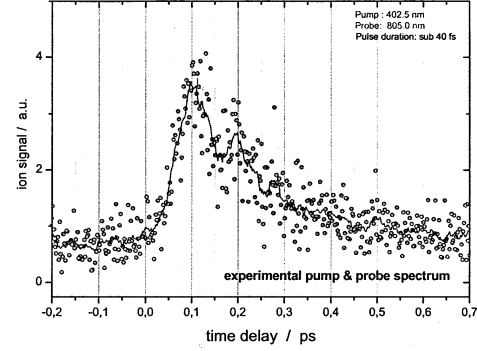
(a) $(\text{CpMn}(\text{CO})_3)^+$ (b) $(\text{CpMn}(\text{CO})_2)^+$ 

Figure 4.16: Experimental spectra: (a) parent ion, $(\text{CpMn}(\text{CO})_3)^+$, and (b) daughter ion, $(\text{CpMn}(\text{CO})_2)^+$, using sub 40 fs (FWHM) pump and probe pulses [129] (dots = original experimental data, solid lines = fits to these data).

One of the main goals of this work is to understand the quantum dynamical processes behind the recent experimental pump-probe spectra (figure 4.16) performed by Wöste and coworkers [129] using ultrashort pump and probe pulses with parameters summarized in table 4.1. The experimental pump (1 photon excitation) and probe (3 photon excitation) pulses have a width of 45 fs (FWHM) and 35 fs (FWHM), respectively. These values correspond approximately to our theoretical \sin^2 -shaped laser pulses (*cf* equation 4.1) with a pulse duration $t_{pulse} = 100$ fs (for a \sin^2 -pulse, $t_{pulse} = 100$ fs corresponds to $\Delta t = 36$ fs FWHM of intensity).

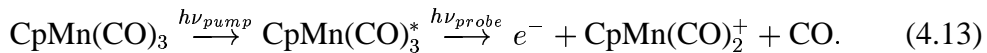
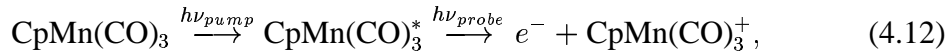
	λ	$\Delta\lambda$	Δt (FWHM)
pump (1 photon)	402.5 nm (3.080 eV)	12 nm (0.092 eV)	45 fs
probe (3 photons)	805.0 nm (1.540 eV)	35 nm (0.067 eV)	35 fs

Table 4.1: Parameters of the experimental pump and probe pulses.

In figure 4.16 the transient spectra probing the parent ion (a), $(\text{CpMn}(\text{CO})_3)^+$, and daughter ion (b), $(\text{CpMn}(\text{CO})_2)^+$, are shown. The solid lines in figure 4.16 are fits to the experimental data (dots). These fits indicate maxima at around 80 fs for

the parent and at around 100 fs for the daughter ion. In both cases further maxima with lower peak intensities occur at later delay times separated by approximately 80-85 fs. This vibrational pattern has not been resolved in previous pump-probe experiments performed using longer pulses ($\Delta t \approx 90$ fs) shown in figure 1.9, where only the decay (but not the vibration) can be seen.

In our one-dimensional model (see Introduction) photoionization of the parent molecule versus dissociation of the first carbonyl ligand and formation of the "daughter-ion" is considered:



In order to theoretically reproduce the experimental results shown in figure 4.16, *ab initio* quantum dynamical wave packet propagations have been carried out calculating the pump-probe spectra as the corresponding yields of populations in the ionic states. All interactions with the different x-, y- and z-components of the molecular transition dipole operators are taken into account, and the total parent or daughter ion signals are calculated as superpositions of the (classically) rotationally averaged (*cf* section 2.3) signals for the individual contributions. The five lowest neutral singlet states a^1A' , b^1A' , c^1A' , a^1A'' and b^1A'' and the three lowest ionic doublet states $(a^2A'')^+$, $(a^2A')^+$, $(b^2A')^+$, are included in the pump-probe simulations and depicted in figure 4.1. As mentioned in section 4.1 low field strengths ($\epsilon_{x/y/z} = 0.5$ GV/m) are employed in the pump-probe simulations in order to avoid unphysical back-transformation of ionic state population. As already reported before, measurable population transfer to the repulsive a^1A'' state requires high intensities ($\gg 0.5$ GV/m) because of the weak transition dipole moment of this excited state. Therefore, only excitations (pump) to the b^1A'' , b^1A' , and c^1A' states were considered (see figure 4.11). As described in the previous sections, the b^1A'' , b^1A' and c^1A' states are populated predominantly by x-, y- and z-polarized lasers, respectively, and no selection rules hold for transitions from the neutral excited to the ionic states.

Subsection 4.5.1 studies the pump-probe spectra using y- and z-polarized pump lasers which transfer the main part of the population to the b^1A' and the c^1A' states, respectively. The resulting spectra, however, cannot reproduce the experimental outcome (figure 4.16). Starting with a leading pump excitation to the b^1A'' state (x-pol.) a pump-probe mechanism will be described in subsection 4.5.2 which yields a good agreement with the experiment. Based on this *analysis* of the experimental pump-probe spectra (figure 4.16) an experimental optimal control pulse [129] which produces predominantly parent ions will be translated into the language of laser-driven wave packets in subsection 4.5.3 (*control*).

4.5.1 Pump probe spectra with pump transitions to the b^1A' and c^1A' states

In this subsection the influence of pumping predominantly the b^1A' (y-pol.) and the c^1A' (z-pol.) states on the pump-probe spectrum is investigated. According to our results reported in section 4.1 the nonadiabatic coupling between these states can be neglected.

Let us first consider the resulting pump-probe spectra after a pump pulse with resonant $a^1A' \rightarrow b^1A'$ excitation energy, $\hbar\omega = 3.23$ eV, corresponding to a 1-photon excitation, analogous to the experiment (*cf* table 4.1). Due to the chosen pump frequency, the y-polarized part of the laser mainly populates the b^1A' neutral excited state while the c^1A' , and b^1A'' states, preferentially excited by z- and x-polarized pulses, respectively, show negligible populations in our simulations.

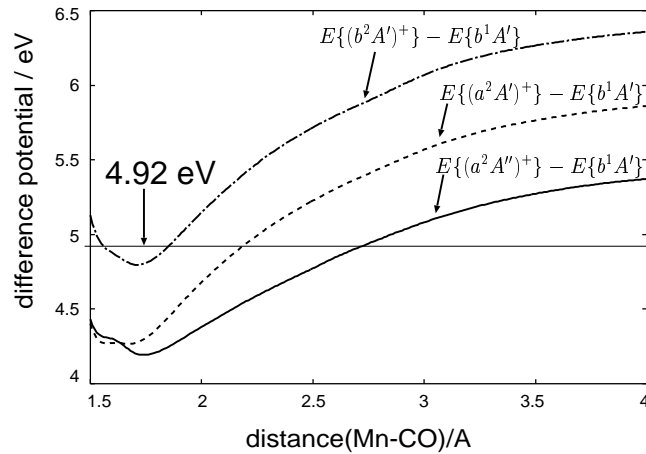


Figure 4.17: Difference potentials between the state b^1A' and the ionic states $(a^2A'')^+$ (solid line), $(a^2A')^+$ (dashed line) and $(b^2A')^+$ (dot-dashed line).

A single-photon probe energy of $\hbar\omega = 4.92$ eV corresponds to 3 photons with energy 1.64 eV (note that the experiment employs 3 photons with energy 1.54 eV, see table 4.1) and is in resonance with all the three ionic states at different points according to the difference potentials shown in figure 4.17. Consequently, the wave packet in the b^1A' state is probed by the 4.92 eV pulse to the $(b^2A')^+$ ion at ca. 1.85 Å, to the $(a^2A')^+$ ion at ca. 2.2 Å and to the $(a^2A'')^+$ ion at ca. 2.8 Å. For transitions at these points the transition dipole moment is largest for the population transfer to the $(a^2A')^+$ ionic state (see figure 3.15). As a consequence, the transitions to this ionic state are the ones governing the resulting overall pump-probe signal depicted in figure 4.18. Indeed, the contributions to the other ionic states are negligible with the present laser parameters and the overall rotationally averaged pump-probe signal is dominated by the contribution of the $(a^2A')^+$ ion.

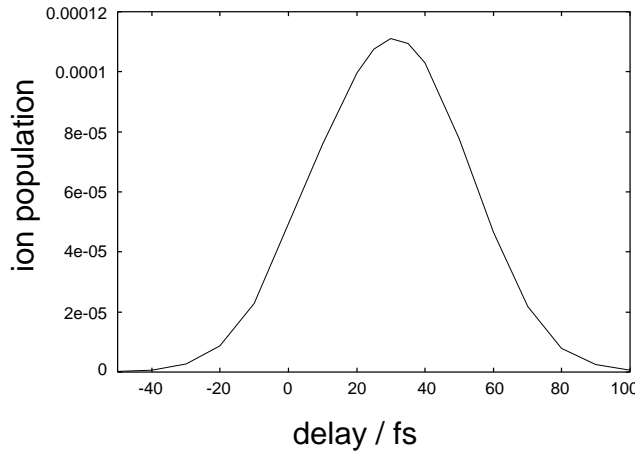


Figure 4.18: Theoretical pump-probe spectrum using a pump energy of 3.23 eV (1 photon) and probe energy 3.92 eV (1 photon). The overall rotationally averaged signal is governed by the ion population in the $(a^2 A')^+$ state resulting from a pump excitation to the $b^1 A'$ neutral excited state and a probe of this state at around 2.2 Å to the $(a^2 A')^+$ ion.

As expected, the repulsive $b^1 A'$ yields a fast rising and decaying pump-probe signal shown in figure 4.18, which is not able to explain the much slower decay present in the experiment (*cf* 4.16). The daughter ion would be produced when the wave packet transferred from the repulsive $b^1 A'$ to any ionic state has enough kinetic energy (which is according to the Franck-Condon principle conserved during vertical transitions) to overcome the dissociation barrier in the ionic state. In the present case the barrier height in the $(a^2 A')^+$ ionic state is about 0.9 eV at 2.2 Å, but where the wave packet in the $b^1 A'$ is probed it has a kinetic energy of only 0.5 eV. Therefore, using the probe frequency 4.92 eV the wave packet has not enough kinetic energy to climb the barrier and thus only the parent ion is produced.

Probe pulses with higher energies would induce the dissociating $b^1 A'$ wave packet at later times when it has higher kinetic energies and consequently can overcome the ionic state barrier to yield the daughter ion. For instance, a probe laser energy of 5.85 eV corresponds to a resonant $b^1 A' \rightarrow (a^2 A')^+$ excitation at around 4 Å. At this point the kinetic energy (≈ 0.6 eV) is larger than the barrier (0.07 eV) and, therefore, the daughter would be observed in our computer simulations. However, the probe energy 5.85 eV corresponds to 3×1.95 eV, a much higher value than the experimental one (*cf* table 4.1), and is, therefore, not considered here.

Note that the total ionic signal (max. $\approx 0.01\%$) is a factor of ten smaller than the maximal ion populations in the following pump-probe spectra with pump excitations to the $b^1 A''$ or $c^1 A'$ state. This implies that contributions from the y-component can be neglected provided off-resonant pump energies to the $b^1 A'$ state

are used, since it would result in even smaller ion populations.

Next, let us turn to investigate the pump-probe spectra resulting from employing a 1-photon pump laser of 3.49 eV energy and a 4.716 eV (1 photon corresponding to 3×1.572 eV) probe pulse. Under these conditions the x- and y-components of the pump pulse do not contribute to the overall rotationally-averaged pump-probe signal since the pump frequency is strongly off-resonant to the b^1A' and b^1A'' states (nearly 1 eV to the b^1A'' and more than 1.5 eV to the b^1A' state). Consequently, only the c^1A' state will be excited by the pump.

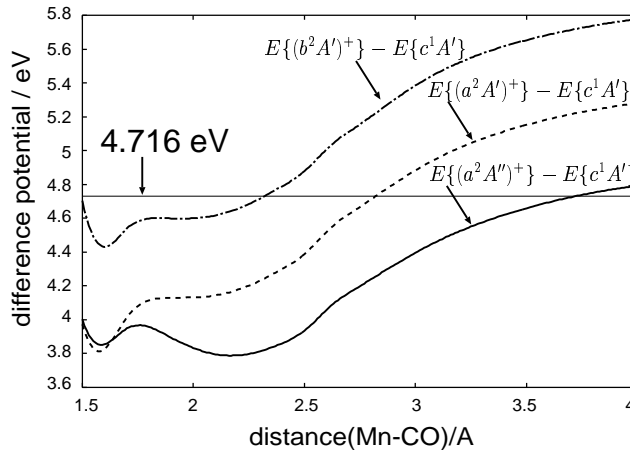


Figure 4.19: Difference potentials between the state c^1A' and the ionic states $(a^2A'')^+$ (solid line), $(a^2A')^+$ (dashed line) and $(b^2A')^+$ (dot-dashed line).

As shown in figure 4.19 the probe pulse (4.716 eV) is resonant to the $(b^2A')^+$ ionic state at ca. 2.3 Å, slightly before the barrier maximum of the c^1A' neutral excited state, and at values larger than 2.5 Å to the other two ionic states, $(a^2A')^+$ and $(a^2A'')^+$. A big part of the wave packet is trapped in the potential well of the c^1A' state and thus can not be probed to the energetically lower ionic states because these ionic states are resonant only after the barrier. In addition, the transition dipole moment corresponding to the $c^1A'-(b^2A'')^+$ transition is larger than those to the other ionic states (see figure 3.16). Therefore, contributions from the a^2A'' and b^2A'' ions are negligible and the only ionic state that contributes to the pump-probe signal shown in figure 4.20 is the energetically highest ionic state, $(b^2A'')^+$.

According to the pump frequency, the main part of the wave packet is trapped in the c^1A' potential, but releases population each time it reaches the barrier centered around 2.3 Å. The resulting slowly decaying signal shows maxima at 85 fs and 260 fs and minima at 180 fs and 360 fs. This vibrational pattern with a full period of about 200 fs does not reproduce the experimental oscillation period of 85 fs though (*cf* 4.16). According to the spectrum shown in figure 4.20, a delay of 85

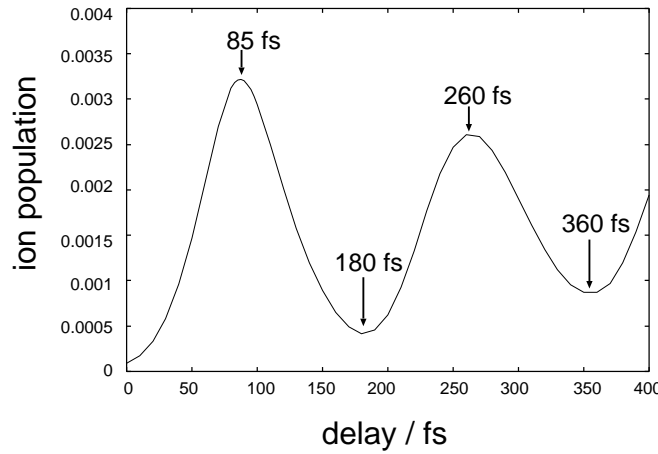


Figure 4.20: *Pump probe spectrum using a y-polarized pump laser of energy = 3.49 eV and probe at 4.716 eV. Shown is the overall spectrum dominated by the $c^1 A'$ $\rightarrow (b^2 A'')^+$ probe transition around 2.3 Å.*

fs (first maximum), could produce predominantly the parent ion. This is an anticipation of our proposed optimal control mechanism, which is described in detail in section 4.5.3.

	photon energy	t_{pulse}	$\epsilon_{x/y/z}^0$	leading TDM
pump (1 photon)	3.43 eV	100 fs	0.5 GV/m	x-pol
probe (1 photon)	4.852 (3×1.617) eV	100 fs	0.5 GV/m	-
pump (1 photon)	3.23 eV	100 fs	0.5 GV/m	y-pol
probe (1 photon)	4.920 (3×1.640) eV	100 fs	0.5 GV/m	-
pump (1 photon)	3.49 eV	100 fs	0.5 GV/m	z-pol
probe (1 photon)	4.716 (3×1.572) eV	100 fs	0.5 GV/m	-

Table 4.2: *Parameters of the theoretical, \sin^2 -shaped (cf equation (4.1)) pump and probe pulses.*

Finally let us consider a x-polarized pump pulse which excites predominantly the $b^1 A''$ neutral state nonadiabatically coupled with the repulsive $a^1 A''$ state. It has been found that the pump frequency 3.43 eV achieves this target and with a photon energy of 4.852 eV the bound $b^1 A''$ neutral state is probed at 1.80 Å yielding the parent ion. Simultaneously the nonadiabatically coupled, repulsive $a^1 A''$ state is probed at ca. 2.3 Å producing the daughter ion. With the chosen pump also the $c^1 A'$ state (z-pol.) is significantly populated but the probe, 4.852 eV, is off-resonant from $c^1 A'$ to all ionic states and, therefore, the z-component of the pump laser will not contribute to the overall pump-probe spectrum. This mechan-

ism will be described in detail in the next section. But before, the applied pump and probe pulse parameters of our theoretical simulations are summarized in table 4.2.

4.5.2 Analysis: Theoretical and experimental pump-probe spectra of the parent and the daughter ion

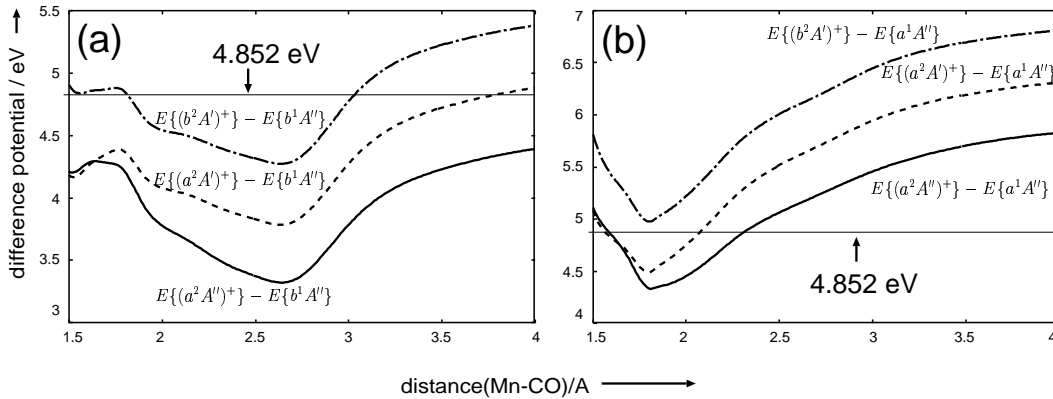


Figure 4.21: Panel (a): Difference potentials between the state $b^1 A''$ and the ionic states $(a^2 A'')^+$ (solid line), $(a^2 A')^+$ (dashed line) and $(b^2 A')^+$ (dot-dashed line). Panel (b): Difference potentials between the state $a^1 A''$ and the ionic states $(a^2 A'')^+$ (solid line), $(a^2 A')^+$ (dashed line) and $(b^2 A')^+$ (dot-dashed line).

In this section pump and probe energies leading to spectra governed by the dynamics in the excited neutral state $b^1 A''$ are considered. The pump and probe pulses are chosen as 3.430 eV and 4.852 eV, corresponding to single photon excitation and ionization, respectively. The excitation energy for the theoretical pump pulse, 3.430 eV, is slightly larger than the experimental value, 3.080 eV, due to an energetic shift of the potential energy curves of the excited states, given the accuracy of the *ab initio* calculations (0.2-0.3 eV) [130].

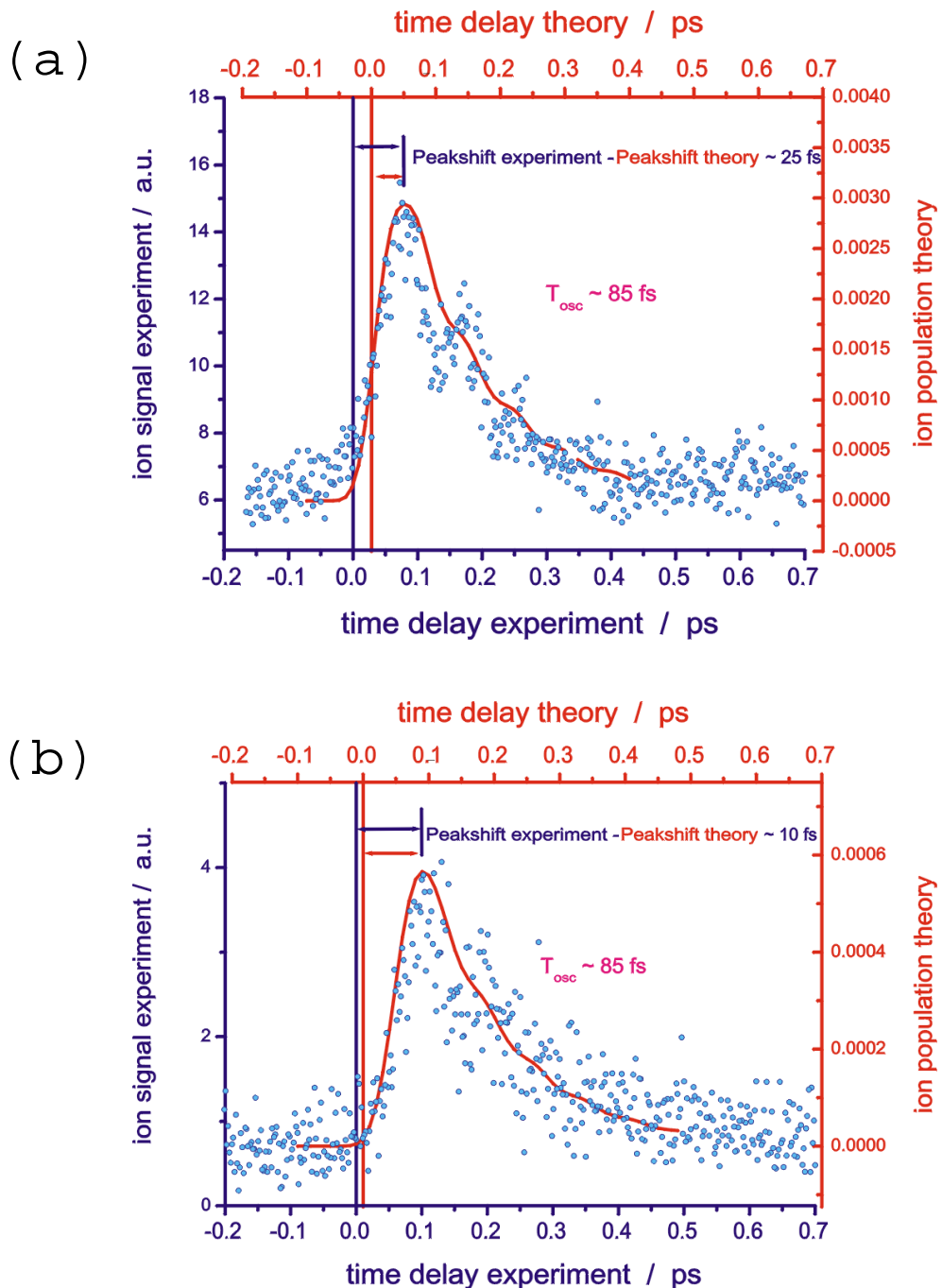


Figure 4.22: Theoretical (lines) and experimental (dots) pump-probe spectra: (a) Parent ion ($\text{CpMn}(\text{CO})_3^+$). (b) Daughter ion ($\text{CpMn}(\text{CO})_2^+$). The kinetic coupling terms are scaled by a factor 0.75 in the theoretical simulations. The energies of the pump and probe pulses of 100 fs duration are 3.430 eV and 4.852 eV, respectively (see table 4.2).

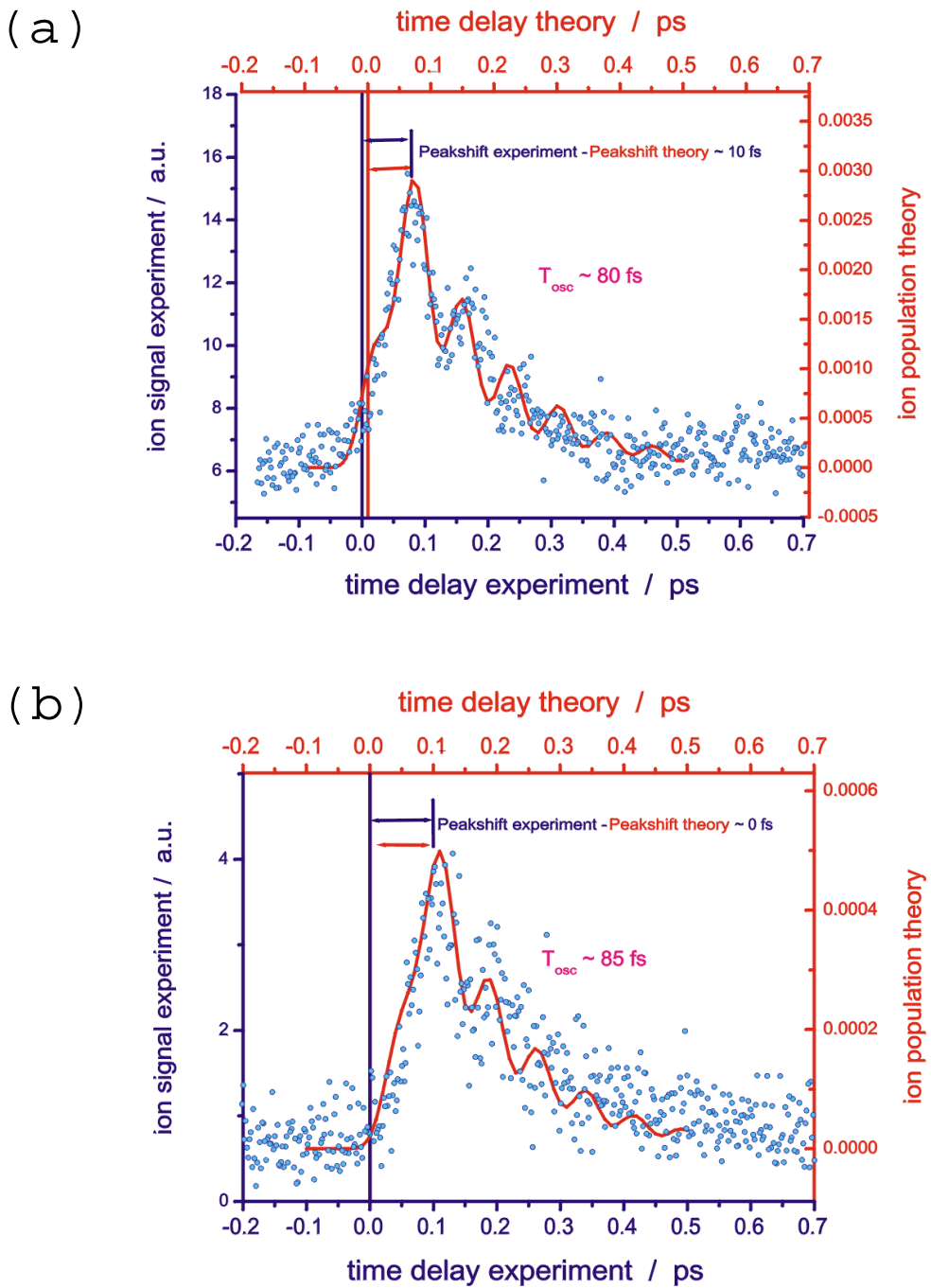


Figure 4.23: Theoretical (lines) and experimental (dots) pump-probe spectra: (a) Parent ion ($CpMnCO_3^+$). (b) Daughter ion ($CpMnCO_2^+$). The kinetic coupling terms are scaled by a factor 0.75 in the theoretical simulations and, in addition, the ground state potential is shifted by 0.04 Å to the left leading to a more pronounced oscillation pattern compared with figure 4.22. The energies of the pump and probe pulses of 100 fs duration are 3.430 eV and 4.852 eV, respectively (see table 4.2).

Likewise, the energy difference between the theoretical single-photon and experimental three-photon ionization probe pulses i.e. $4.852 - 3 \cdot 1.540 = 0.232$ eV is due, in part, to an energetic shift of the potential energy curves of the ion with respect to the neutral excited states; another part may also be absorbed as mean kinetic energy of the photo-detached electron (ZEKE approximation, section 2.5).

The probe is plotted in figure 4.21 showing the difference potentials between the $b^1 A''$ and the ionic states. As already mentioned at the end of the previous section, the vibrating wave packet in the bound $b^1 A''$ is probed on the left turning point of the vibration at around 1.8 Å and the $a^1 A''$ is probed at 2.3 Å leading to a simultaneous measurement of the parent and daughter ion signal. The probe pulse corresponds to computationally more demanding simulations of three-photon ionization processes with carrier photon energies, 1.715 eV.

The resulting theoretical pump-probe spectra (lines) of the parent and the daughter ion are shown in figure 4.22 together with the experimental results (dots) depicted already in figure 4.16. The kinetic couplings used to model the pump-probe spectrum have been scaled by the factor 0.75 since using the original couplings (*cf* figures 3.10 and 3.12) cannot reproduce the experimental decay times and time shifts of the parent- and daughter-ion signals. This scaling is justified by possible errors of the kinetic coupling terms (see section 3.6.3).

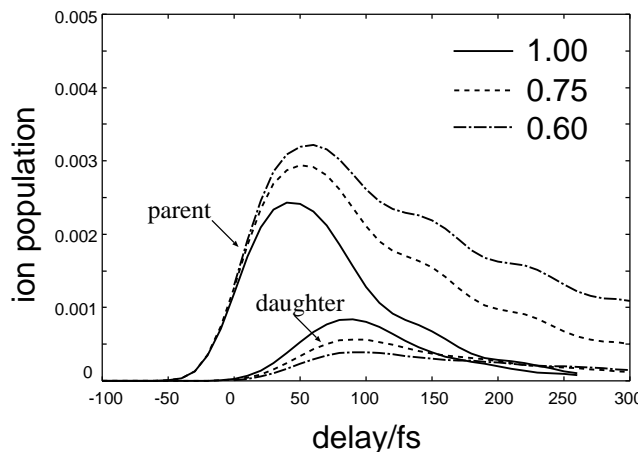


Figure 4.24: Parent- (upper three curves) and daughter-ion signals (lower three curves) for different scaling of the kinetic coupling terms: 1.00 (solid lines) corresponds to the original data presented in figures 3.10 and 3.12. 0.75 (dashed lines) and 0.60 (dot-dashed lines): The original couplings are multiplied by a factor 0.75 and 0.60, respectively. The energies of the pump and probe pulses of 100 fs duration are 3.430 eV and 4.852 eV, respectively (see table 4.2).

Figure 4.24 shows the pump-probe signal of the parent ion for different scaling factors: 1.00 (original data), 0.75 and 0.60. Obviously, a smaller kinetic coup-

ling leads to a slower decay and to a slight shift of the parent- and daughter-signal maxima towards larger delay times (in better agreement with the experiment). Furthermore, the maximum of the parent signal is smallest when using the original coupling, but largest when using a scaling factor of 0.60. The inverse holds for the daughter ion signals. The theoretical parent and daughter ion signal (*cf* figure 4.22 or 4.24 with scaling factor 0.75) show maxima at 55 fs and at 90 fs, respectively. These values correspond to peak shifts with respect to the experiment (exp. parent maximum at 80 fs and exp. daughter maximum at 100 fs) of 25 fs and 10 fs, respectively. The decaying signal has further, less intense maxima which occur with a period of 80 fs. This vibrational pattern, however, is much less pronounced in the theoretical spectrum than in the experimental one. Therefore, the MR-CCI ground state potential $a^1 A'$ has been slightly shifted by 0.04 Å to the left corresponding to the shift of the MR-CCI minimum to the minimum of the CASSCF $a^1 A'$ potential. This leads to a more pronounced vibrational pattern in the theoretical parent and daughter ion signals. The resulting theoretical spectra depicted in figure 4.23 show a better agreement with the experimental ones. The first maxima now appear at 70 fs for the parent ion and at 100 fs for the daughter ion, corresponding to peak shifts with respect to experiment of 10 fs and 0 fs, respectively. The oscillation period still has a value of 80 fs. The decay time $\tau = 166$ fs has been evaluated by fitting an

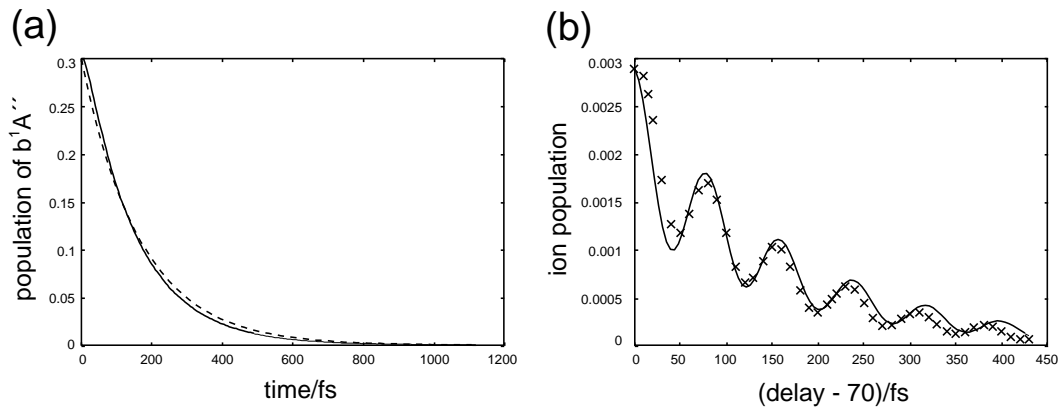


Figure 4.25: Panel (a): Nonadiabatic decay of the $b^1 A''$ population (solid line) and corresponding exponential fit (dashed line) with decay time $\tau = 166$ fs. The vibrational ground state wave function of the $b^1 A''$ state has been employed as the initial wave function. Panel (b): Fit of the theoretical pump-probe signal of figure 4.23 (dots) by the function (4.14). The pump-probe data are shifted 70 fs to the left so that the peak of the first maximum is located at delay time zero.

exponential to the time-dependent population of the $b^1 A''$ state (*cf* figure 4.25(a)). The $b^1 A''$ population decays due to the $b^1 A''$ - $a^1 A''$ kinetic coupling which has been

scaled by 0.75. This decay time corresponds to 45 fs (± 10 fs) after deconvolution of the laser pulse form [127]. The pump-probe signal depicted in figure 4.23 can be fitted by the following function:

$$f(x) = \left(0.00209 \cdot \exp\left(-\frac{t_{delay}}{166}\right) \right) \cdot \left(1 + 0.0389 \cdot \cos\left(\frac{2\pi}{80} \cdot t_{delay}\right) \right), \quad (4.14)$$

where the first factor contains the exponential decay, $\tau = 166$ fs, and the second factor involves the oscillatory pattern with a period of 80 fs. This function is shown in figure 4.25(b) together with the theoretical pump-probe data which have been shifted 70 fs to the left so that the peak of the first maximum is located at delay time zero.

The time evolution of the laser driven system is simulated by representative wave packets which move on, and carry out transitions between the adiabatic potential energy curves. In figure 4.26 snapshots of these wave packets at different propagation times t are depicted.

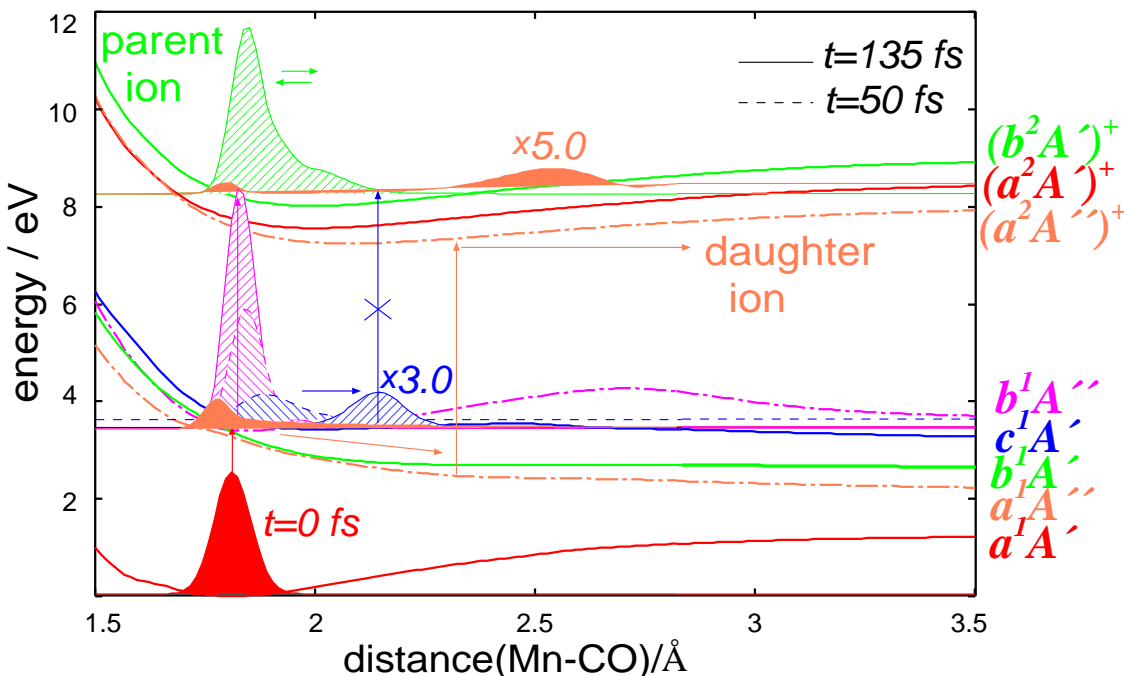


Figure 4.26: Analysis of the pump-probe mechanism. The excited and ionic states wave packets have been enlarged with respect to the ground state by factors 30 and 1000, respectively. In addition the wave packets on the $c^1 A'$ and the $(a^2 A'')^2$ potentials have been scaled by a factor of 3 and 5, respectively. The energies of the pump and probe pulses of 100 fs duration are 3.430 eV and 4.852 eV, respectively (see table 4.2).

To translate the propagation times (for instance those in figure 4.26) into delay times between the pump and probe pulse the following points must be taken into

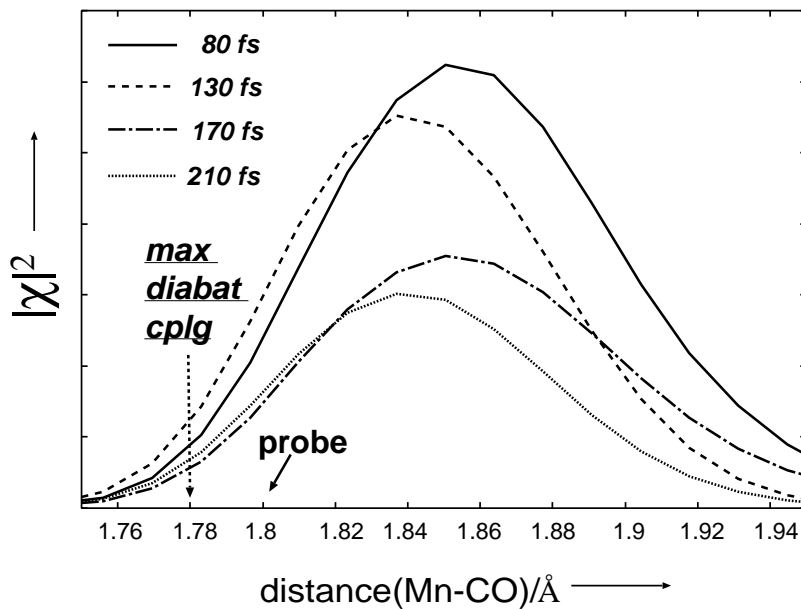


Figure 4.27: Snapshots of the wave packet in the b^1A'' state at 80, 130, 170 and 210 fs. The energies of the pump and probe pulses of 100 fs duration are 3.430 eV and 4.852 eV, respectively (see table 4.2).

consideration: In our propagations the pump pulse always starts at propagation time $t = 0$. If the wave packet should be probed at a certain point (for example where the probe pulse is resonant to an ionic state) at a certain time, e.g. $t=100$ fs, the probe pulse should have the maximum intensity at that propagation time (100 fs). Since the maximum of a 100 fs \sin^2 -pulse appears at 50 fs the probe pulse should start 50 fs before the wave packet reaches the resonance point at $t = 100$ fs (where a maximal amount of population is transferred to the ionic state). Consequently, a maximum will appear in the pump-probe spectrum, in the given example, at a delay time of $100-50$ fs = 50 fs. Vice versa, a maximum at a delay time of 50 fs points to a resonant transition at propagation time $t = 100$ fs (in the same example).

The underlying mechanism of the pump-probe experiment is derived from analysis of the wave packet dynamics for the simulated spectra: Exemplarily, consider the case of the time delay of 85 fs between the pump (3.430 eV, $t_{pulse} = 100$ fs) and probe (3.852 eV, $t_{pulse} = 100$ fs) pulses, as suggested by the time delay of the first maximum of the pump-probe spectrum in figure 4.20 (z-pol.) which is the basis of our interpretation of the experimental control pulse in the following subsection. This delay time, 85 fs, clearly belongs also to the first maximum of the spectrum depicted in figure 4.23 (x-pol.). The corresponding laser induced dynamics is illustrated by snapshots of the dominant densities of the wave packets at propagation

times $t = 0$ fs (initial state), $t=50$ fs (peak of the pump pulse), and $50 + 85 = 135$ fs (peak of the probe pulse) in figure 4.26. Accordingly, the pump pulse (which has 3.430 eV photon energy in the theoretical simulation) prepares $\text{CpMn}(\text{CO})_3$ preferably in two excited states *i.e.* the c^1A' and b^1A'' states, by means of interactions with the z- and x-components of the transition dipoles, respectively.

Consider first the effects of the laser induced dynamics in the b^1A'' state. As soon as the pump pulse excites the b^1A'' state, the corresponding partial wave packet starts to vibrate with 80 fs oscillation period. Simultaneously it decays non-adiabatically, by means of kinetic couplings, to the dissociative a^1A'' state. Snapshots of this decaying wave packet are depicted in figure 4.27. At propagation time $t=80$ fs the maximum of the population in the b^1A'' state is reached. Probing the wave packet in the center (around 1.85 Å) should yield a maximum in the pump-probe spectrum at a delay time of $80-50 = 30$ fs. However, in our simulation the wave packet is probed at 1.80 Å (around the left turning point) and as a consequence the maximum appears when the wave packet reaches this turning point at propagation time $t=130$ fs, which corresponds to the maximum at delay time $130-50 = 80$ fs in the pump-probe spectrum. Another maximum appears at propagation time $t = 210$ fs (delay time: $210-50 = 160$ fs) and another minimum at 170 fs (delay time: $170-50 = 120$ fs), which corresponds to the wave packet at the left and right turning point, respectively.

The formation and oscillatory decay of this partial wave packet in the b^1A'' state is monitored by the probe pulse (with 4.852 eV photon energy in the theoretical simulation) which prepares the parent ions $(\text{CpMn}(\text{CO})_3)^+$ by a transition to the potential well of the second excited ion state, b^1A' . The phenomenon of oscillatory ion signals resulting from oscillatory broad wave packets has been noted in a previous work by Engel [131]. Moreover, the same pattern is also imposed on the density of the complementary wave packet which is transferred nonadiabatically from the b^1A'' state to the a^1A'' state, where it dissociates towards the fragments, $\text{CpMn}(\text{CO})_2 + \text{CO}$. The probe pulse (4.852 eV) transfers a small fraction of this dissociative wave packet from the a^1A'' state to the ground state of the ion, producing thus daughter ions, $(\text{CpMn}(\text{CO})_2)^+$.

As a consequence, the oscillatory decay pattern of the parent ion signal appears also in the daughter ion, with approximately the same oscillation period of ca. 80 fs (the vibrational period of the b^1A'' state), but with a shift between the peaks (30 fs) of the theoretical parent and daughter ion spectra due to the time needed by the wave packet in the a^1A'' state to travel from its origin, close to the dominant diabatic transition at 1.78 Å to the Franck-Condon window for the probe at 2.3 Å.

Next, consider the effects of the wave packet in the c^1A' state - these are much simpler than those taking place in the coupled b^1A'' and a^1A'' states. After prepar-

ation by the pump pulse, the partial wave packet in the c^1A' state vibrates releasing part of its population each time it reaches the barrier centered around 2.5 Å. The wave packet is probed at a delay time of 85 fs, corresponding to the first (most intense) maximum in the pump-probe spectrum (figure 4.20), what is incidentally nearly the 80 fs vibrational period of the wave packet in the b^1A'' potential well. At this delay time (85 fs), corresponding to a propagation time of 135 fs in figure 4.26, the wave packet reaches the right turning point but is not transferred to any ionic state because the probe pulse (4.852 eV) turns out to be off-resonant from transitions from the c^1A' state to any ionic states. Consequently, according to the presented mechanism the z-polarized part of the pump laser will not contribute to the overall pump-probe signal.

As we will see, the analysis of the pump-probe spectra in terms of the underlying laser induced molecular processes is essential for predicting the mechanism of optimal control described in the next subsection.

4.5.3 *Control: Wave packet dynamics induced by the optimal control pulse for $(\text{CpMn}(\text{CO})_3)^+$*

Based on the theoretical simulations of the experimental pump-probe spectra in the previous subsections we are now ready to derive the quantum dynamical processes induced by the experimental optimal pulse designed to maximize the parent ion, $(\text{CpMn}(\text{CO})_3)^+$, and shown in figure 4.28. This pulse results from a multi-photon optimization experiment where a single laser beam centered at a wavelength of around 800 nm (1.55 eV) with spectral width of $\Delta\lambda = 8\text{-}10 \text{ nm}$ (0.016-0.019 eV), the reference pulse, passes across a pulse shaper setup, which allows the simultaneous modulation of phase- and amplitude. The outcoming optimal pulse (*cf* figure 4.28) which controls the production of the parent ion consists of two dominant sub-pulses followed by a third, marginal one, with ca. 85 fs time delays. Figure 4.28 also shows the phase which changes little around the first two sub-pulses. The maximum of the phase between the second and the third sub-pulse possesses no physical importance since the intensity in that region is nearly zero.

Using the phase ϕ the chirp can be calculated according to [132]:

$$\omega = \omega_0 - \frac{d\phi}{dt}, \quad (4.15)$$

where ω_0 is the carrier frequency of the reference pulse¹. Fitting the phase of the

¹Note that in the literature the negative sign in equation (4.15) is sometimes replaced by a positive one, for instance see ref. [133].

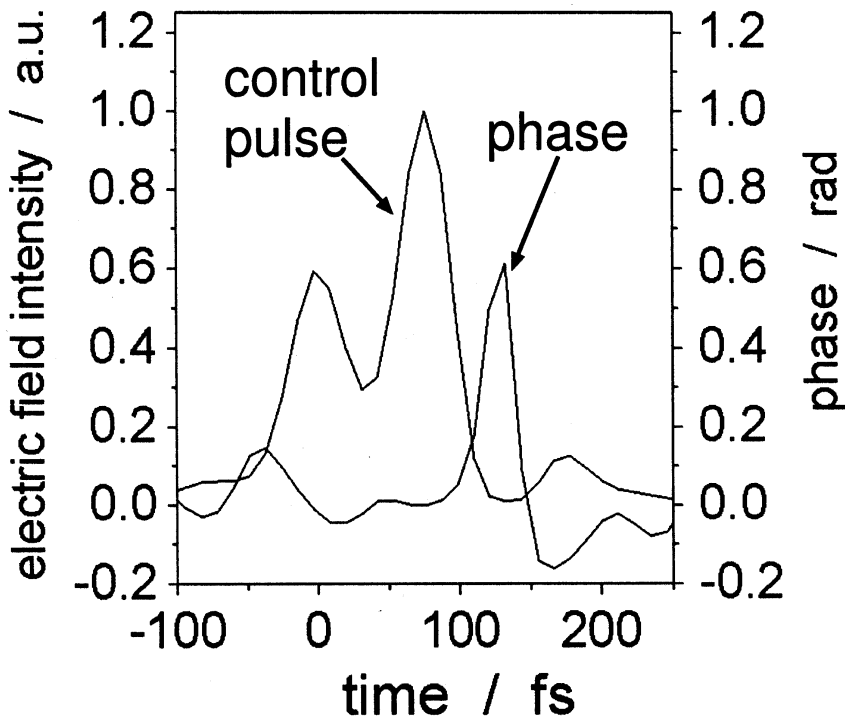


Figure 4.28: *Experimental optimal control pulse and corresponding phase [129].*

three sub-pulses (see figure 4.28) with a polynomial function, one gets [129]:

$$\text{first sub-pulse: } \phi = -0.00821 - 0.0036 \cdot t + 6.98955 \cdot 10^{-5} t^2 + 6.55448 \cdot 10^{-7} t^3 \quad (4.16)$$

$$\text{second sub-pulse: } \phi = -1.85989 \cdot 10^{-4} + 7.79724 \cdot 10^{-4} \cdot t + 6.21517 \cdot 10^{-5} \cdot t^2 \quad (4.17)$$

$$\text{third sub-pulse: } \phi = -0.13866 + 0.00226 \cdot t + 8.99761 \cdot 10^{-5} \cdot t^2 \quad (4.18)$$

As a result from the linear term in the polynomial expansion of the phase, $-0.0036 \cdot t$, the first sub-pulse has a slightly higher central frequency than the original pulse. The value of this blue-shift $\hbar\Delta\omega = 0.0024$ eV corresponds to ca. 0.16 % of the reference frequency (1.55 eV). Resulting from the linear term ($7.79724 \cdot 10^{-4} \cdot t$) the second sub-pulse is slightly red-shifted by 0.0006 eV Furthermore, both, the first ("pump") and the second ("probe") sub-pulses show a slight linear down-chirp with values $\Delta\phi = 2 \cdot 6.98955 \cdot 10^{-5} \cdot t$ and $\Delta\phi = 2 \cdot 6.21517 \cdot 10^{-5} \cdot t$, respectively. But these linear chirps have a negligible effect on the pump-probe spectrum, as test calculations have shown.

The wave packet dynamics induced by the optimal laser pulse can be understood by means of a careful analysis of the pump-probe spectrum shown in figure 4.20. This spectrum shows a first and most intense maximum at a delay time of 85 fs, which is also the delay times between the three sub-pulses of the optimal control pulse (*cf* figure 4.28). The pump and probe energies in that case have been 3.49 eV and 4.716 eV, respectively (see table 4.2) and, as explained in subsection 4.5.1, the pump (z-pol.) and probe pulses induce predominantly $a^1A' \rightarrow c^1A'$ and $c^1A' \rightarrow (b^1A')^+$ transitions, respectively. Accordingly, we assume that the optimal pulse achieves the target, *i.e.* increasing the preparation of parent ions by hindering fragmentation, in two dominant sequential steps: First, selective excitation to the c^1A' neutral state (first sub-pulse); and second, selective ionization to the $(b^1A')^+$ ionic state (second sub-pulse), followed by a third, less important step (third sub-pulse). Since the third sub-pulse has a much lower intensity than the other two sub-pulses, it has only marginal effects not included in the following theoretical simulations.

The dominant effects of the first and second sub-pulses of the optimal laser pulse are demonstrated by simulation of the wave packet dynamics, illustrated in the snapshots shown in figure 4.29. The experimental two- and three-photon excitation (first sub-pulse) and ionization (second sub-pulse) are represented in the theoretical simulations by single photon processes with mean photon energies $3.490 (2 \times 1.745 \text{ eV}) \text{ eV}$ and $4.716 (3 \times 1.572) \text{ eV}$. The effect of the two sub-pulses are contained in figure 4.29 and they can be explained as follows: The first sub-pulse must avoid excitation of state b^1A'' since this state would decay nonadiabatically to the dissociative a^1A'' state, causing competing preparations of parent as well as daughter ions, channels (4.12) plus (4.13) after the second sub-pulse (see previous subsection, *analysis*). Instead, the first sub-pulse should excite exclusively the c^1A' state which does not decay to any dissociative state, on the time scale of the optimal laser pulse. For this first purpose, the laser pulse optimization should generate the first sub-pulse consisting of the high-frequency components of the reference pulse. In our theoretical simulation, a slightly higher pump energy more in resonance with the c^1A' state than the previous "analysis" pump has been employed. In the simulation describing the control we used a pump energy of 3.49 eV = $2 \times 1.745 \text{ eV}$ and in the one describing the pump-probe spectrum we used 3.43 eV = $2 \times 1.715 \text{ eV}$. The pump pulse in our control experiment has, therefore, a 0.03 (per photon) $\times 2 \text{ eV} = 0.06 \text{ eV}$ higher energy than in the analysis experiment of the pump-probe spectra (previous subsection).

The second sub-pulse probes the wave packet in the c^1A' state slightly before it reaches the barrier at around 2.5 Å at a time delay of 85 fs corresponding to a propagation time of 135 fs in figure 4.29. After this time delay the population in

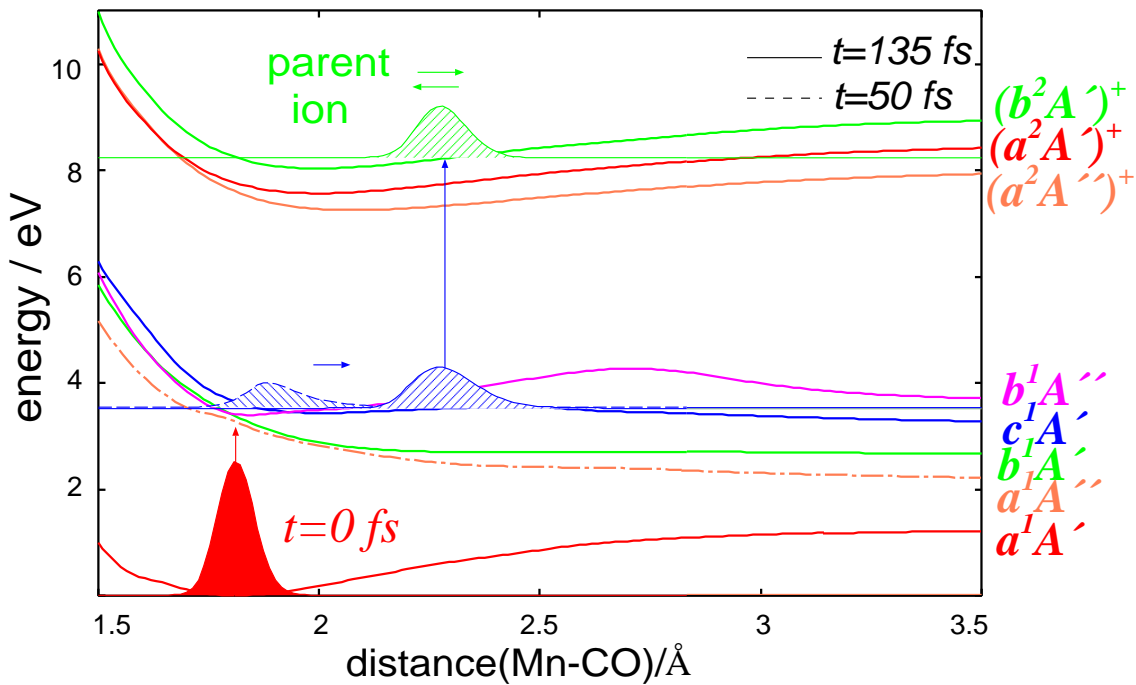


Figure 4.29: *Hypothetical control mechanism.* The excited and ionic states wave packets have been enlarged with respect to the ground state by factors 30 and 1000, respectively. The first and second sub-pulse of the optimal control pulse (cf figure 4.28) are simulated by "pump" and "probe" pulses with photon energies 3.49 eV and 4.716 eV, respectively.

the c^1A' state will decay as can be seen from the pump-probe spectrum in figure 4.20 and, therefore, a later preparation of parent ions (analogous to probing) would be less efficient. To be resonant with the $(b^1A')^+$ ionic state the probe (second sub-pulse) needs to have a lower energy than in our previous analysis simulation, which was 4.852 eV. In our theoretical simulation of the control mechanism a probe energy of 4.716 eV has been employed corresponding to a theoretical shift of -0.136 eV or $3 \times (-0.045)$ eV in a 3-photon excitation.

Due to the frequencies employed, the described mechanism leads in our theoretical simulation to a nearly exclusive production of the parent ion, whereas in the experiment the obtained mass peak ratios $\text{CpMn}(\text{CO})^+/\text{CpMn}(\text{CO})_3^+$ has been 1:13 before and 1:16 after optimization [24] corresponding to an increase of parent ions but not to a complete optimization. This incompleteness is due to the small spectral width (8-10 nm) of the reference pulse which does not allow a modulation to higher pump (first sub-pulse) energies, which would produce better resonance with the bound c^1A' state.

Note that the energies in the pump-probe experiment are $2 \times$ or $3 \times$ 1.54 eV (805 nm) but the carrier frequency in the control experiment is $2 \times$ or $3 \times$ 1.55

eV (800 nm). The experimental blue-shifts of the pump (2 photons) and probe (3 photons) are thus 0.02 eV and 0.03 eV, respectively. In addition, the pump energy is blue-shifted by 2×0.0024 eV and the probe is re-shifted by 3×0.0006 eV compared to the reference pulse energy, as calculated above using the fitted optimal phase. Therefore, the overall experimental blue-shift of the pump sub-pulse in figure 4.28 compared with the previous pump in table 4.1 is $2 \times (0.01 + 0.0024) = 2 \times 0.0124$ eV which corresponds to 0.8 % of the pump energy in the pump-probe simulation. The probe sub-pulse of the optimal control experiment is blue-shifted by $3 \times (0.01 - 0.0006)$ with respect to the probe energy given in table 4.1.

The experimental and theoretical shifts are summarized in table 4.3. The theoretical blue-shift of the pump energy (2×0.03 eV) and red-shift of the probe energy (3×0.045 eV) are three and four times larger in absolute value than the experimental pump (2×0.0124 eV) and probe (3×0.0094 eV) shifts, respectively. This difference between theory and experiment accounts in part for a relative shift of the potential energy curves (*e.g.* A' vs. A'' or neutral excited vs. ionic states). Another part may also be due to the fact that the proposed theoretical mechanism exclusively produces parent ions, whereas in the experiment the yield of parent ions is only maximized as much as the narrow spectral range of the reference pulse (8-10 nm) allows.

$\text{pump}^{\text{exp}}(\text{control}) - \text{pump}^{\text{exp}}(\text{analysis})$ (2 photons)	$2 \times (0.01 + 0.00124)$ eV
$\text{probe}^{\text{exp}}(\text{control}) - \text{probe}^{\text{exp}}(\text{analysis})$ (3 photons)	$3 \times (0.01 - 0.0006)$ eV
$\text{pump}^{\text{theo}}(\text{control}) - \text{pump}^{\text{theo}}(\text{analysis})$ (2 photons)	2×0.03 eV
$\text{probe}^{\text{theo}}(\text{control}) - \text{probe}^{\text{theo}}(\text{analysis})$ (3 photons)	$3 \times (-0.045)$ eV

Table 4.3: Experimental (exp) and theoretical (theo) shifts of the pump and probe energies in control vs. analysis.

The quantitative and qualitative effects of the third sub-pulse are marginal, yet complex, in comparison with the dominant first and second sub-pulses. On the one hand, a small fraction of the wave packet in the $c^1 A'$ state which was not ionized by the second sub-pulses could vibrate back to the left turning point of the $c^1 A'$ potential well. There it would be transferred into parent ions in the second ionic excited state by the third sub-pulse. On the other hand, a fraction of the original wave packet in the electronic $a^1 A'$ ground state which was not excited by the first sub-pulse could be excited to the repulsive $b^1 A'$ state by the second sub-pulse. Before complete dissociation, part of that partial wave in the $b^1 A'$ state would be trapped as parent ions by the third sub-pulse, without producing any daughter ions.

In conclusion, the mechanism of the optimal laser pulse for producing predominantly parent ions $\text{CpMn}(\text{CO})_3^+$, channel (4.12), has been discovered after care-

fully analyzing high resolution pump-probe signals by means of quantum dynamical simulations based on *ab initio* potentials. The analysis has been facilitated by the rather simple pattern of the optimal laser pulse consisting of two dominant sub-pulses plus a third marginal one. The first sub-pulse is supposed to act as a pump-pulse populating in as much as possible the $c^1 A'$ state. After a delay of about 85 fs the second sub-pulse (probe) transfers the $c^1 A'$ population to the $(b^1 A')^+$ ionic state to form the parent ion. Starting from the reference pulse, the laser optimization generates two dominant sequential sub-pulses where the pump has slightly higher and the probe has slightly lower frequencies than in the previous pump-probe spectrum in order to yield the target ion (via the excited $c^1 A'$ state) while suppressing the competing channel (here: via the excited $b^1 A''$ state).

The present analysis may also be extended for predictions of optimal pulses for the daughter ion $\text{CpMn}(\text{CO})_2^+$: The pump pulse should have a lower central frequency than the reference pulse to populate predominantly the low-lying repulsive $b^1 A'$ state. Subsection 4.5.1 studies the pump-probe spectra using a pump laser of energy 3.23 eV which transfer the main part of the population to this state. The wave packet in the $b^1 A'$ state, see discussion in subsection 4.5.1, would prepare the daughter ion provided the probe energy is high enough to mainly transfer it to the $(a^2 A'')^+$ ionic state at a delay time which corresponds to enough kinetic energy to overcome the ionic states barrier. Thus, lower pump and much higher ionization (probe) frequencies are necessary to achieve this target, *i.e.* optimizing the daughter ion yield. The excitation to the $b^1 A'$ state involves also an alternative way of producing the parent ion. As has been discussed in section 4.5.1, the pump and probe energies of 3.23 eV and 3.92 eV, respectively, mainly produce the parent ion (*cf* figure 4.18).

The present shift of the ground state minimum (0.04 Å) and the scaling of the the kinetic couplings ($\times 0.75$) are within quantum chemical accuracy. The shift and scaling correspond to an "inversion" of the experimental pump-probe and control spectra from which we have extracted information to fit the theoretical signals to the experimental ones. Additional experimental and theoretical studies may serve to fix other parameters *e.g.* the vertical excitation energies of the excited and ionic states.